Statistics of bubble plumes generated by breaking surface waves

Morteza Derakhti[1], Jim Thomson[1], Christopher Bassett[1], Mika Malila[2], and James T. Kirby[3]

[1]Applied Physics Laboratory, University of Washington, Seattle, WA, USA
[2]Institute of Marine Sciences, University of North Carolina at Chapel Hill, Morehead City, NC, USA
[3]Center for Applied Coastal Research, Department of Civil and Environmental Engineering, University of Delaware, Newark, DE, USA

Key Points:

- Bubble plumes generated during ocean surface wave breaking are observed with echosounders on drifting buoys.
- Bubble plume depths are well correlated with whitecap coverage, wind speed, and spectral wave steepness.
- Bubble plumes persist for many wave periods and exceed the persistence of visible surface foam.

Corresponding author: Morteza Derakhti, `derakhti@uw.edu`

Abstract

We examine the dependence of the penetration depth and fractional surface area (e.g., white-cap coverage) of bubble plumes generated by breaking surface waves on various wind and wave parameters over a wide range of sea state conditions in the North Pacific Ocean, including storms with sustained winds up to 22 m s^{-1} and significant wave heights up to 10 m. Our observations include arrays of freely drifting SWIFT buoys together with shipboard systems, which enabled concurrent high-resolution measurements of wind, waves, bubble plumes, and turbulence. We estimate bubble plume penetration depth from echograms extending to depths of more than 30 m in a surface-following reference frame collected by downward-looking echosounders integrated onboard the buoys. Our observations indicate that mean and maximum bubble plume penetration depths exceed 10 m and 30 m beneath the surface during high winds, respectively, with plume residence times of many wave periods. They also establish strong correlations between bubble plume depths and wind speeds, spectral wave steepness, and whitecap coverage. Interestingly, we observe a robust linear correlation between plume depths, when scaled by the total significant wave height, and the inverse of wave age. However, scaled plume depths exhibit non-monotonic variations with increasing wind speeds. Additionally, we explore the dependencies of the combined observations on various non-dimensional predictors used for whitecap coverage estimation. This study provides the first field evidence of a direct relation between bubble plume penetration depth and whitecap coverage, suggesting that the volume of bubble plumes could be estimated by remote sensing.

Plain Language Summary

Quantifying the statistics of bubble plumes generated during ocean surface wave breaking is essential to understanding the exchange between the ocean and the atmosphere. Bubble plumes also cause important variations in underwater acoustics and optics. Recent studies also suggest that the statistics of bubble plumes are skillful predictors for total energy loss during wave breaking, which is an essential quantity for accurate wave forecasting. In this study, we examine how these bubble plume statistics change with different wind and wave conditions, including during storms. We used echosounders on drifting buoys to detect the bubbles and estimate how deep they go in the ocean. We also used shipboard camera systems to measure the surface area of the bubble plumes. We successfully develop multiple empirical relationships that allow us to predict how bubble plume depth and surface area change as a function of simple wind and wave statistics. These statistics are readily available from existing forecast models or typical ocean buoys. Our findings reveal that bubble plume depth is correlated with its visible surface area. This intriguing correlation suggests that we might estimate the volume of bubble plumes simply by observing the ocean surface from above.

1 Introduction

Air-entraining breaking surface waves play a significant role in air-sea exchanges of mass, heat, energy, and momentum [*Melville*, 1996; *Sullivan and McWilliams*, 2010; *Deike*, 2022], and are also crucial in various technical applications, such as the design of marine structures and underwater communications. Breaking waves inject a relatively large volume of air into the water column as bubbles which then form intermittent bubble clouds at a wide range of spatial scales, hereafter referred to as bubble plumes. The entrained bubbles change the optical properties of the water column [*Terrill et al.*, 2001; *Al-Lashi et al.*, 2016] and generate acoustic noise [*Felizardo and Melville*, 1995; *Manasseh et al.*, 2006], especially during the active breaking period.

Quantifying the statistics of these bubble plumes (*e.g.,* void fractions, size distributions, penetration depth, surface area, and volume of bubble plumes averaged over many waves) is essential to obtain robust parameterizations of fluxes at the ocean-atmosphere interface and variations in underwater acoustics and optics. Recent studies, including the present

observations, also show that the statistics of bubble plume that represent the overall size of bubble plumes are strongly correlated with total wave breaking dissipation [*Schwendeman and Thomson*, 2015a; *Callaghan et al.*, 2016; *Callaghan*, 2018; *Derakhti et al.*, 2020a]. This suggests that such bubble plume statistics are skillful predictors for the corresponding energy and momentum exchange between the ocean and atmosphere, especially in high sea states.

The statistics representing the overall size of bubble plumes for a given sea state may be defined, in a wave-averaged sense, as the long-time (several minutes) average of the surface area and the penetration depth of individual bubble clouds. The former may be directly approximated from whitecap coverage W, representing the average visible surface area of bubble plumes and surface foam patches per unit sea surface area. W is a reasonably easily measurable quantity using optical video systems. Estimation of bubble plume depth is, however, challenging and rare, especially during active wave breaking period. This study provides concurrent observations of W and bubble plume penetration depth in various sea states.

Many previous studies have examined the dependence of W on wind speeds and sea states [*Monahan and Muircheartaigh*, 1980; *Callaghan et al.*, 2008; *Kleiss and Melville*, 2010; *Schwendeman and Thomson*, 2015a; *Brumer et al.*, 2017; *Malila et al.*, 2022]. Despite large scatter in the data, particularly for wind speeds less than 10 m s^{-1}, these recent field studies have established fairly consistent empirical formulations that allow for the estimation of W based on specific wind and/or sea state parameters.

Fewer previous studies have reported mean values of the penetration depth of bubble plumes, $\overline{D}_{bp}$, across a range of wind speeds using upward-looking sonars moored to the seabed or a platform [*Thorpe*, 1982, 1986; *Dahl and Jessup*, 1995; *Vagle et al.*, 2010; *Wang et al.*, 2016; *Strand et al.*, 2020; *Czerski et al.*, 2022a,b]. These observations show that $\overline{D}_{bp}$ tends to increase with higher wind speeds, ranging from $[1-5]$ m at low winds to $[7-25]$ m during storms. However, our understanding of the dependence of the statistics of D_{bp} on wind and sea state parameters remains limited.

In general, the evolution of bubble plumes can be characterized into two distinct stages. The first stage involves the rapid injection of bubbles with relatively high void fractions, typically lasting only several seconds, within actively breaking waves. This rapid injection process is closely associated with breaking events. The subsequent stage involves the slower transport of smaller bubbles, typically with diameters below 100 μm, exhibiting much lower void fractions within the surface mixed layer. This transport process occurs over longer timescales and, as discussed in detail below, contributes significantly to the observed depth distribution of bubbles when using sonars.

The main objective of this study is to understand and quantify the statistics characterizing the size of bubble plumes, averaged over many waves (on the order of minutes), generated by breaking surface waves in the open ocean. Our observations include arrays of freely drifting, surface-following SWIFT buoys combined with shipboard wind and optical video systems. This setup enabled us to make concurrent high-resolution measurements of wind, waves, whitecap coverage, bubble plumes, and turbulence across a wide range of sea state conditions in the North Pacific Ocean, including storms with sustained winds up to 22 m s^{-1} and significant wave heights up to 10 m. We estimate bubble plume penetration depth from echograms, collected by downward-looking echosounders integrated onboard the buoys, that extend to depths of over 30 m in a surface-following reference frame.

We focus on examining the dependence of the statistics of the penetration depth of bubble plumes D_{bp} on various wind and wave parameters and the relation between D_{bp} statistics and W. Further, we comment on the role of wind history on W values. In a planned companion paper, we also investigate dynamic relationships between these bubble plume statistics and total wave breaking dissipation using our synchronized observations of bubble plumes and dissipation rates.

The rest of this paper is organized as follows: §2 describes the observed environmental conditions and our analysis for estimating bubble plume penetration depths. §3 describes the dependency of the bubble plume statistics on various wind and sea state parameters. Discussion and a summary of the main findings are provided in §4 and §5, respectively.

2 Methods

2.1 Data

The present dataset includes observations of wind, waves, air and sea temperature, near-surface turbulence, time-depth images of acoustic backscatter (referred to as echograms), above- and subsurface optical imagery obtained by freely drifting surface-following SWIFT buoys [*Thomson*, 2012; *Thomson et al.*, 2019], along with concurrent shipboard measurements of wind, temperature, and whitecap coverage. These data were collected during an 18-day research cruise in the North Pacific Ocean (Figure 1a) in December 2019. The primary objective of the cruise was to conduct concurrent observations of breaking surface gravity waves and the associated bubble plume statistics. The secondary objective involved the replacement of a long-term moored wave buoy at Ocean Station PAPA (50° N, 145° W), which reports as CDIP 166 and NDBC 46246. Hereafter, we refer to the present dataset and cruise with the abbreviation PAPA.

The PAPA cruise, conducted aboard the R/V *Sikuliaq*, departed Dutch Harbor, AK, on 5 December 2019 and ended in Seattle, WA, on 23 December 2019. Arrays of SWIFT buoys were deployed from the ship early in the morning and usually recovered later the same day. Most shipboard and autonomous measurements were conducted during local daylight hours, while eastward transits continued overnight. Figure 1a shows the PAPA cruise track and the average locations of SWIFT buoys during each deployment along the transit. Figures 1b, 1c, and 1d illustrate the wide range of sea state conditions in the PAPA dataset, including U_{10N} (0.8 − 22 m s^{-1}), H_s (2.2 − 10.0 m), $T_m = f_m^{-1}$ (6.6 − 11.6 s), T_p (6.5 − 14.6 s), $T_{air} − T_{sea}$ (−4.4 to 1.2 °C), c_m/U_{10N} (0.6 − 17.5), dU_{10N}/dt (−10.2 to 6.9 m s^{-1}/hr). These conditions encompassed a storm near Station PAPA with sustained wind speeds reaching up to 22 m s^{-1} and significant wave heights up to 10 m. We note that a significant portion of the data was collected in the presence of persistent rain, although rain rates were not measured.

Raw SWIFT data were collected at sampling rates ranging from 0.5 to 5 Hz in bursts lasting 512 seconds, with intervals of 12 minutes. Processed SWIFT data, including wave spectra and bubble plume statistics, are produced for each burst for each buoy. Subsequently, concurrent bursts are averaged among the buoys, typically involving four of them. During the cruise, more than 2000 bursts of data were collected by arrays of two to six SWIFT buoys. A total of 599 processed data points are obtained at 12-minute intervals, spread across 14 daylight deployments. The statistics obtained from the shipboard measurements, such as wind speeds and whitecap coverage, represent 10-minute average values at times that the processed SWIFT data points are produced.

Two versions of SWIFT buoys were concurrently used here, the third generation buoys have uplooking Nortek Aquadopp Doppler sonars [*Thomson*, 2012], and the fourth generation buoys have downlooking Nortek Signature1000 Doppler sonars which enable synchronous measurements of acoustic backscatter (*i.e.*, echograms), broadband Doppler velocity profiles, and high-resolution (HR) turbulence profiles through the near-surface layer [*Thomson et al.*, 2019]. This new SWIFT capability allows us to quantify the penetration depths of bubble plumes in a surface-following reference frame, with raw data capturing the time evolution within individual waves (*i.e.*, phase-resolved).

This section provides a detailed description of the methodologies we use to process echogram data and obtain bubble plume statistics. The instrumentation and methods that are used to obtain the remaining environmental variables and statistics, such as wind speeds, wave spectra, and whitecap coverage, are described in several previous observational studies
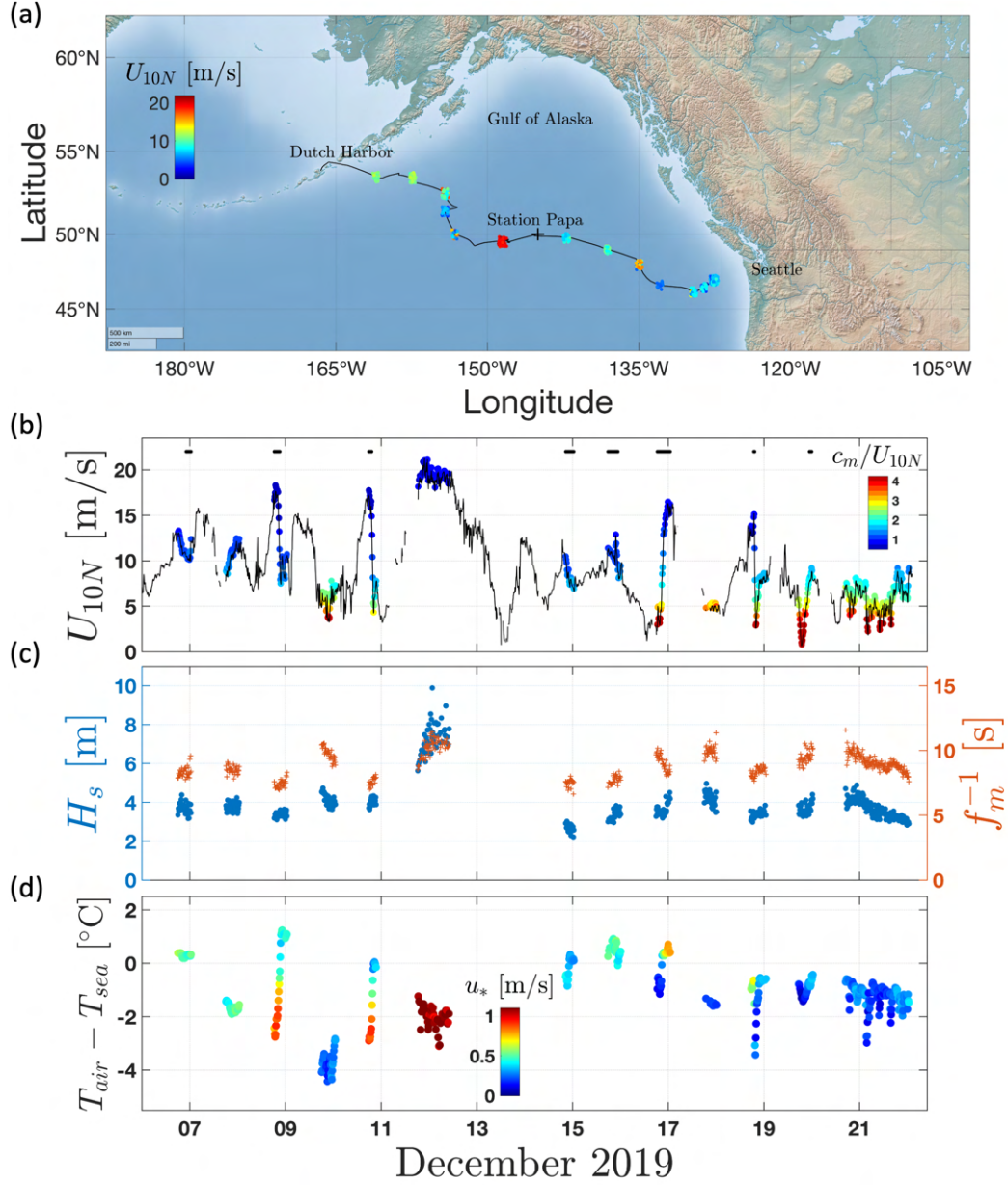
Figure 1: Overview of (*a*) the cruise track (solid line) and average locations of the drifting SWIFT buoys (circles) during each deployment along the transit, and (*b* − *d*) the observed range of environmental conditions. Here U_{10N}, H_s, f_m, T_{air}, and T_{sea} represent 10-minute average neutral wind speed at 10 m above the sea surface, significant wave height, spectrally-averaged wave frequency, and air and water temperature, respectively. The color code in (*b*) and (*d*) shows the wave age and the air-side friction velocity, respectively. In (*b*), the horizontal line segments indicate the intervals during which data were collected in the presence of persistent rain (rain rates were not measured). Local water depths during most of the deployments were greater than 4000 m.

167 [*Thomson*, 2012; *Schwendeman and Thomson*, 2015a; *Thomson et al.*, 2016, 2018], and will
168 be briefly summarized here for convenience.

2.2 Wind Statistics

170 We calculate the neutral 10-m wind speed U_{10N} (Figure 1b) following the method out-
171 lined by *Hsu* [2003] from wind speed measurements at 10 Hz, which are corrected for ship
172 motion and airflow distortion. These measurements were obtained by three shipboard sonic
173 anemometers (Metek Omni-3) at approximately 16.5 m height above the sea surface. The
174 mean U_{10N} values are obtained from 10-minute bursts of raw data. We note that the atmo-
175 spheric stability $(T_{air} - T_{sea})$ effect is often neglected when estimating 10-m wind speed. Al-
176 ternatively, U_{10N} is sometimes approximated using the mean wind profile power law, given
177 by $U_{10}^{PL} = U_z (10/z)^{1/7}$. Figure 1b shows the observed range of shipboard measurements
178 for $U_{10}^{PL} = U_{16.5} (10/16.5)^{1/7}$ (solid line) and the estimated U_{10N} values (circles). These
179 estimates are provided for the times the processed SWIFT data are produced.

180 During the PAPA cruise, the atmospheric stability was predominantly negative, with
181 $T_{air} - T_{sea}$ ranging between -4.4 °C and 1.2 °C, as shown in Figure 1d. These values indicate
182 unstable atmospheric boundary layer conditions. Figure 2a illustrates that, in unstable atmo-
183 spheric conditions, U_{10N} values are larger than U_{10}^{PL} by a margin ranging from 2% to 30%.
184 These differences tend to decrease with increasing wind speed or higher $T_{air} - T_{sea}$ values.
185 Furthermore, Figure 2a demonstrates that the discrepancies between U_{10N} and U_{10}^{PL} values
186 remain within 2% for stable atmospheric conditions (*i.e.*, $T_{air} - T_{sea} > 0$).

187 The friction velocity u_* of the airflow can be readily estimated using a modified log-
188 arithmic mean wind profile [*Hsu*, 2003], which accounts for atmospheric stability effects.
189 Additionally, the air-side friction velocity is independently estimated using the inertial dis-
190 sipation method, assuming neutral atmospheric stability, as described in *Thomson et al.*
191 [2018]; *Yelland et al.* [1994]. However, robust estimates of u_* are only achieved for a frac-
192 tion of the time due to the strict requirements that the ship's heading is within 60 degrees
193 of the wind and that the turbulent wind spectra match an expected frequency to the power
194 of $-5/3$ shape. Figure 2b presents the two estimates of u_* against U_{10N} during the PAPA
195 cruise, with mean u_* values calculated over 10-minute bursts. For reference, the correspond-
196 ing data from *Schwendeman and Thomson* [2015a], where u_* values were estimated using the
197 inertial dissipation method, are also compiled in Figure 2b. Note that, for all relevant anal-
198 yses in this study, we use the u_* values obtained from the modified logarithmic mean wind
199 profile method [*Hsu*, 2003].

2.3 Wave Statistics

201 Wave spectral information, which includes the wave power spectral density $E(f)$ (m²
202 s) and the frequency-dependent directional spread $\Delta\theta(f)$, is obtained from a combination of
203 GPS and IMU measurements collected by the SWIFT buoys. These measurements cover the
204 frequency range of $0.01 - 0.49$ Hz with a resolution of 0.012 Hz, as described in *Schwen-
205 deman and Thomson* [2015a]; *Thomson et al.* [2018]. As detailed below, several bulk and
206 spectral wave parameters are then calculated using $E(f)$ and $\Delta\theta(f)$.

207 Figure 2c shows examples of the observed $E(f)$, color-coded based on the correspond-
208 ing U_{10N} values, for $U_{10N} > 10$ m s^{-1}. The two vertical dotted lines in Figure 2c denote the
209 equilibrium range, defined by *Schwendeman and Thomson* [2015a], which spans from $\sqrt{2} f_m$
210 to $\sqrt{5} f_m$. In this frequency range, the spectra approximately decay as f^{-4}, consistent with
211 the observations of *Schwendeman and Thomson* [2015a]. Here, f_m represents the spectrally-
212 weighted mean frequency, calculated as

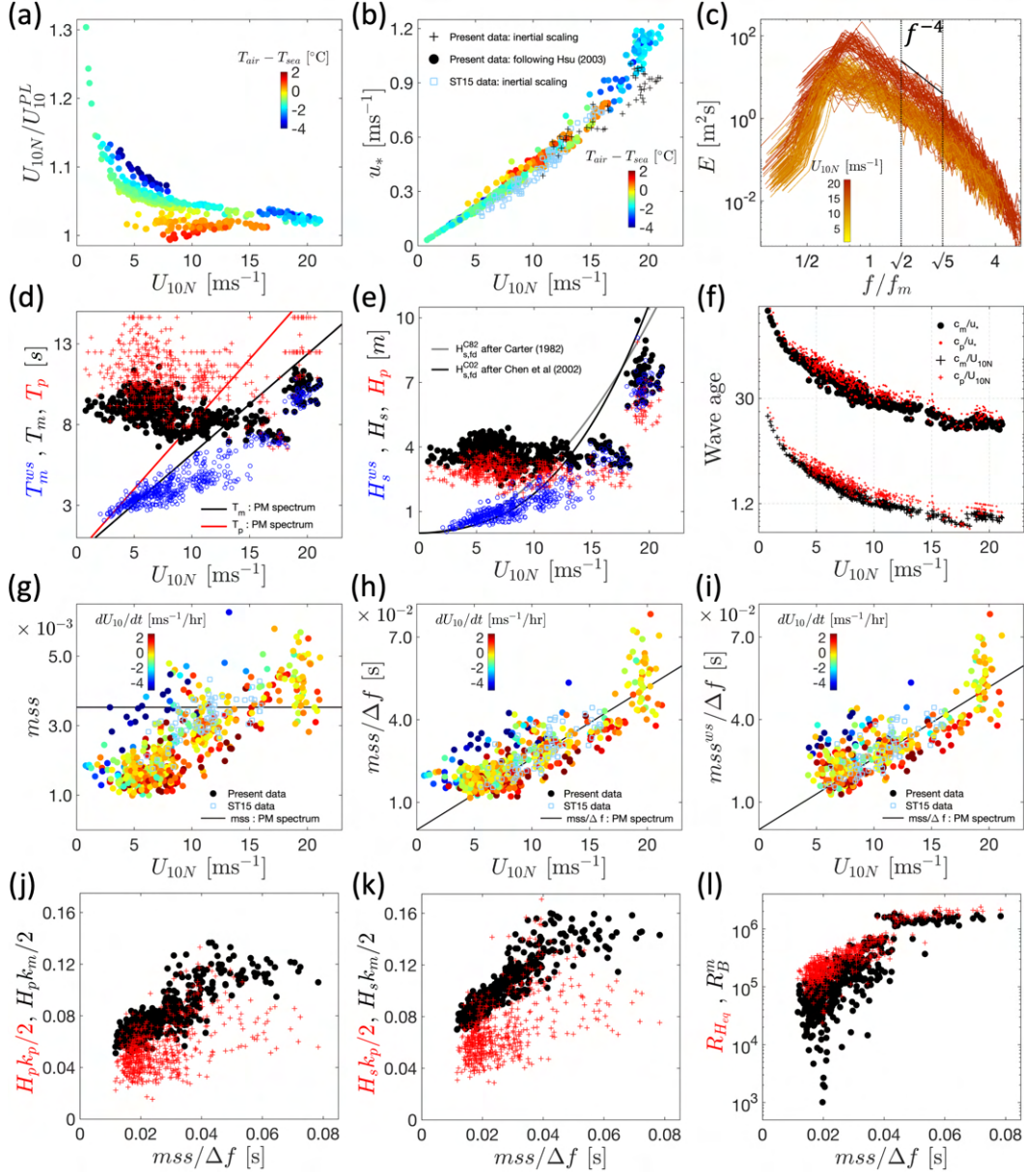$$f_m = \frac{\int f E(f) df}{\int E(f) df}. \tag{1}$$

Figure 2: Observed range of wind and wave statistics against U_{10N} [m / s] and equilibrium-range mean square slope $mss/\Delta f$ [s] (Eq. 2). All variables are defined in §2.2 and §2.3.

213 Figure 2d shows the observed range of two commonly used alternatives for a characteristic
214 wave period T, the peak wave period $T_p = f_p^{-1}$ and the mean wave period $T_m = f_m^{-1}$ (Eq. 1),
215 as a function of U_{10N}. Figure 2d also shows the wind sea mean wave period $T_m^{ws} = (f_m^{ws})^{-1}$,
216 where f_m^{ws} calculated as given by Eq. 1 but over the wind sea portion of the observed wave
217 spectra $E^{ws}(f)$. Here $E^{ws}(f)$ is estimated using a 1D wave spectral partitioning technique
218 following *Portilla et al.* [2009]. The solid lines in Figure 2d represent the T_m and T_p values
219 predicted by the Pierson-Moskowitz spectrum, a representative spectrum of fully developed
220 wind-driven seas.

221 Figure 2e shows the observed range of several characteristic wave heights as a function
222 of U_{10N}, with $H_s = 4(\int E(f)df)^{1/2}$ the total significant wave height, $H_P = 4(\int_{0.7f_p}^{1.3f_p} E(f)df)^{1/2}$
223 a peak wave height (after *Banner et al.* [2000]), and $H_s^{ws} = 4(\int E^{ws}(f)df)^{1/2}$ the wind
224 sea significant wave height. Two estimates of the significant wave height of fully developed
225 seas $H_{s,\text{fd}}$ (solid lines) given by *Carter* [1982] and *Chen et al.* [2002] are also plotted in Fig-
226 ure 2e. Results shown in Figures 2d and 2e indicate that significant swell is present at moder-
227 ate and calm winds in the PAPA data.

228 Several estimates of the corresponding wave age are presented in Figure 2f, where c_p
229 and c_m are the wave phase speeds corresponding to f_p and f_m, respectively. These results
230 show that a significant portion of the PAPA data at high winds ($U_{10N} \geq 15\text{m s}^{-1}$) are char-
231 acterized as developing seas ($c_p/u_* < 30$ or $c_p/U_{10N} < 1.2$), and that equilibrium seas
232 ($c_p/u_* \approx 30$ or $c_p/U_{10N} \approx 1.2$) are mostly observed at moderate winds.

233 It is generally accepted that the wave steepness (or slope), defined as $S = Hk/2$ with
234 H and k being a characteristic wave height and wavenumber, is the most relevant local geo-
235 metric wave parameter to characterize surface gravity wave breaking and related processes in
236 deep water [*Perlin et al.*, 2013]. Several formulations have been proposed to quantify a rep-
237 resentative wave steepness in a wave-averaged sense which are either defined based on wave
238 spectral information [*Banner et al.*, 2002] or bulk wave parameters [*Banner et al.*, 2000].

239 A measure of mean square slope (mss) over a frequency range $f_1 \leq f \leq f_2$, as pro-
240 posed by *Banner et al.* [2002], is calculated as

$$mss = \int_{f_1}^{f_2} k^2 E(f)df = \int_{f_1}^{f_2} \frac{(2\pi f)^4}{g^2} E(f)df, \tag{2}$$

241 and is shown to be a skillful spectral steepness parameter for predicting wave breaking statis-
242 tics in the open ocean [*Schwendeman and Thomson*, 2015a; *Brumer et al.*, 2017]. Many field
243 observations of the speed of visible breaking wave crests [*Phillips et al.*, 2001; *Melville and*
244 *Matusov*, 2002; *Gemmrich et al.*, 2008; *Thomson and Jessup*, 2009; *Kleiss and Melville*,
245 2010; *Sutherland and Melville*, 2013; *Schwendeman et al.*, 2014] have shown that most of
246 surface gravity wave breaking occurs at frequencies noticeably greater than the frequency at
247 the peak of $E(f)$, f_p, with most frequent breaking occurring at $\approx 2f_p$. We note that f_m/f_p
248 varies between 0.9 and 1.6 in the PAPA data (Figure 2d) where most of the f_m/f_p values are
249 within a range $(1.1 - 1.4)$, and that the Pierson-Moskowitz spectrum gives $f_m/f_p \approx 1.30$.
250 Following *Schwendeman and Thomson* [2015a], here we take an equilibrium range mss cal-
251 culated over a frequency range $\sqrt{2}f_m \leq f \leq \sqrt{5}f_m$ ($2k_m \leq k \leq 5k_m$, $c_m/\sqrt{5} \leq c \leq c_m/\sqrt{2}$),
252 which is related to an average spectral steepness of a significant portion of visible breaking
253 waves, especially in developed and equilibrium sea states.

254 Figures 2g and 2h show the variation of the equilibrium range mss and $mss/\Delta f$ ($\Delta f =$
255 $(\sqrt{5} - \sqrt{2})f_m$) against U_{10N}, all color-coded based on the corresponding wind acceler-
256 ations dU_{10N}/dt defined as the rate of change of U_{10N} over 1.5 hr, in the PAPA data to-
257 gether with the corresponding data from *Schwendeman and Thomson* [2015a]. Figures 2g
258 and 2h also show the corresponding values that are obtained from the Pierson-Moskowitz
259 spectrum, which is a representative spectrum of a fully developed sea under constant wind
260 ($dU_{10N}/dt = 0$), given by $[mss]_{PM} \approx 0.436\alpha$ ($\alpha = 8.1 \times 10^{-3}$) and $[mss/\Delta f]_{PM} \approx$
261 $\pi \alpha g^{-1} U_{10N}$. Figures 2g also shows that the observed equilibrium range mss in equilibrium,

developing, and old seas are, on average, consistent with, greater, and smaller than those predicted by the Pierson-Moskowitz spectrum, respectively. Further, our observations corroborate the analytical relations obtained from the Pierson-Moskowitz spectrum, *i.e.*, equilibrium range mss is independent of wind speeds and $mss/\Delta f \propto U_{10N}$ in fully developed seas with constant winds. Further, Figure 2i shows the corresponding wind sea $mss^{ws}/\Delta f$ values where mss^{ws} is calculated as given by Eq. 2 but using $E^{ws}(f)$ over a frequency range $\sqrt{2}f_m \leq f \leq \sqrt{5}f_m$.

Schwendeman and Thomson [2015a] and *Brumer et al.* [2017] used a normalized mss parameter, $mss/(\Delta f \Delta \theta)$, where $\Delta \theta$ is the average of $\Delta \theta(f)$ over $\sqrt{2}f_m \leq f \leq \sqrt{5}f_m$ and reported a decrease of data scatter in their plots of whitecap coverage against $mss/(\Delta f \Delta \theta)$ compared to mss. At any given wind speed, the $mss/(\Delta f \Delta \theta)$ values in the present data are, on average, greater than those in *Schwendeman and Thomson* [2015a] despite consistent mss and mss/Δf values in both datasets. We note that $mss/(\Delta f \Delta \theta)$ can not be defined in a long-crested wavefield or from a 1D wave spectrum. We further note that $\Delta \theta$ is sensitive to the type of buoy and method of processing [*Donelan et al.*, 2015], such that values may not be directly comparable between datasets. Here we avoid the directional normalization and choose the equilibrium range $mss/\Delta f$ as a representative measure of spectral steepness of dominant breaking waves.

The observed range of several bulk steepness parameters, including the significant spectral peak steepness $H_p k_p/2$ (after by *Banner et al.* [2000]) and the significant wave steepness $H_s k_p/2$, against $mss/\Delta f$ are shown in Figures 2j and 2k. Here the peak k_p and mean k_m wave numbers are obtained from the linear gravity wave dispersion relation given by $k = (2\pi)^2 g^{-1} T^{-2}$. Consistent with the literature, we consider these bulk steepness parameters here.

Finally, several dimensionless bulk parameters with general forms of

$$R_H = u_* H/\nu_w, \tag{3}$$

and

$$R_B = u_*^2/(2\pi T^{-1} \nu_w), \tag{4}$$

where $\nu_w \approx 1.4 \times 10^{-6}\,\mathrm{m^2\,s^{-1}}$ is the kinematic viscosity of seawater for $T_w \approx 9\,°C$, are considered. These parameters represent combined effects of wind forcing and wave field and are shown to have skills in predicting oceanic whitecap coverage [*Zhao and Toba*, 2001; *Scanlon and Ward*, 2016; *Brumer et al.*, 2017]. Figure 2l shows the variation of $R_{H_{eq}} = u_* H_{eq}/\nu_w$ and $R_B^m = u_*^2/(2\pi T_m^{-1} \nu_w)$ parameters as a function of the equilibrium range $mss/\Delta f$ in the PAPA data. Here $H_{eq} = 4[\int_{\sqrt{2}f_m}^{\sqrt{5}f_m} E(f)df]^{1/2}$ and $T_m = f_m^{-1}$ are taken as a characteristic wave height H and period T, respectively.

2.4 Whitecap Processing

The whitecap coverage dataset in this study is the same as the North Pacific whitecap coverage dataset described in the recent study by *Malila et al.* [2022]. This section provides a summary of the acquisition and processing of the dataset, much of which is equal or similar in terms of hardware and software to the study by *Schwendeman and Thomson* [2015a].

Visual images of the sea surface were obtained using shipboard video camera systems located on both the port and starboard sides of the vessel. The cameras, of model PointGrey Flea2 equipped with 2.8 mm focal-length lenses, recorded at a rate of 5 to 7.5 frames per second during daylight hours. A total of 60 hours of image data were collected while the ship was stationary, with most of the data coinciding with SWIFT buoy deployments and recoveries. The duration of the video acquisitions varied between 5 and 60 minutes. However, the final mean whitecap coverage W values were obtained over 10 to 20-minute bursts. Each W value represents a 10-minute average of consecutive frames.

The image processing of the grayscale video frames to estimate whitecap coverage closely followed the approach outlined in *Schwendeman and Thomson* [2015a]. First, corrections were applied to account for ship motion induced by waves (*i.e.*, pitch and roll). This correction was achieved using a slightly modified version of the horizon tracking algorithm described in *Schwendeman and Thomson* [2015b]. Subsequently, The stabilized images were geo-rectified and transformed onto regular grids with a resolution of 0.8 m. The whitecap-related foam was isolated from the stabilized, geo-rectified, and gridded frames using the pixel intensity thresholding algorithm described by *Kleiss and Melville* [2011]. The frame-wise fractional whitecap coverage was then computed as the ratio of pixels detected as belonging to whitecaps (given a value of one) to the total number of pixels in the frame. A subset of the original and thresholded frames in each burst was visually quality-controlled for satisfactory image exposure and lens contamination (e.g., raindrops or sea spray). Only image sequences with consistent lighting conditions and minimal lens contamination were included in the final dataset.

2.5 Echogram Processing

Acoustic backscattering data were obtained using the echosounding capabilities of the downward-looking beam of the Nortek Signature1000 Acoustic Doppler Current Profiler (ADCP) mounted on the fourth generation SWIFT buoys. During the PAPA cruise manufacturer firmware version 2205 was used. Sampling frequencies and pulse repetition rates for the echosounder were 1 MHz and one second, respectively. A transmit pulse duration of 500 μs was used. The instrument provided a vertical sampling resolution of 1 cm, covering a depth range of 0.3 m $\leq z_w \leq$ 30.3 m, with z_w being positive downward and $z_w = 0$ representing the instantaneous free surface level after accounting for the depth of the unit on the SWIFTs. The echosounder mode operated in 512-s bursts, collected in the surface-following reference frame, from which echograms are presented. Considering the size of the transducer and the operational frequency, we estimate that the acoustic near-field of the echosounders, defined as in *Medwin and Clay* [1998], extends to less than 1 m. To minimize potential impacts from the acoustic near-field, only data obtained from ranges greater than 1 m from the transducer face are presented (*i.e.*, within the depth range of 1.3 m $\leq z_w \leq$ 30.3 m).

As detailed below, the penetration depths of bubble plumes are estimated based on the volume backscattering strength. Volume backscattering strength S_v [dB re m^{-1}] represents the logarithmic form of the backscattering cross-section per unit volume M_v as given by *Vagle et al.* [2010]. When the signal is dominated by the presence of bubbles, as is the focus in this paper, this is described by

$$
\begin{aligned}
S_v =& 10 \log_{10} M_v = 10 \log_{10} \int_0^\infty \sigma_s(a_b) N(a_b) da_b \\
=& 10 \log_{10}(10^{\frac{Pr}{10}} - 10^{\frac{Nt}{10}}) + 20 \log_{10} r + 2\alpha r + G_{cal} - 10 \log_{10}(\frac{c\tau}{2}) - \phi,
\end{aligned}
\tag{5}
$$

where $\sigma_s(a_b) = 4\pi a_b^2/([(f_R/f)^2 - 1]^2 + \delta^2)$ [m^2] is the scattering cross-section for a bubble with radius a_b [m] and $N(a_b)$ is the bubble size distribution. The use of the upper limit of integration (infinity) is consistent with prior formulations [e.g., *Vagle and Farmer*, 1992] and is retained here. However, in practice, there is typically a practical limit to the maximum bubble size, and this theoretical limit can be replaced with a term representing the maximum bubble size. The terms in this integral represent an important aspect of acoustic scattering from bubbles, which is strongly dependent on bubble size and frequency due to the presence of a strong resonance peak. At sea level, this strong resonance peak occurs at $ka_b \sim 0.0136$, where k is the acoustic wavenumbers [*Medwin*, 1977a]. While acoustic scattering is strongest at resonance, scattering at higher frequencies is driven by the geometric cross-section. In cases involving relatively large bubbles, this off-resonance scattering can even exceed the backscattering contributions from higher densities of smaller bubbles. Thus, the observed acoustic backscattering at a given frequency is generally determined by the combined contributions from the entire size distribution of bubbles.

In practical applications, acoustic scattering is typically measured using instruments like echosounders, which operate at a single frequency or across a specific frequency spectrum. The third representation in Eq. 5 corresponds to the implementation of the sonar equation, where Pr represents the received signal including noise, Nt denotes the noise threshold, r is the range from the transducer to the scattering source, α represents the attenuation coefficient, c is the speed of sound in the water, τ is the transmit pulse duration, ϕ corresponds to the equivalent beam angle of the transducer, and G_{cal} is a gain factor that accounts for a configured transmit power level of the transducer (see Appendix A for additional details). G_{cal} was determined by using standard calibration techniques commonly used for echosounders [*Demer et al.*, 2015]. In practice, Pr represents the received intensity of the signal scattering by the distribution of bubbles in keeping with the integral representation, while the remaining terms represent bookkeeping consistent with system operations and sound propagation. We note that we identified issues with the saturation of the signals associated with system gains during calibration. This results in saturated signals at short ranges when measured backscattering intensity is high, thereby truncating the dynamic range of the system at the upper end. A more comprehensive discussion of this issue can be found in Appendix A. Future versions of the instrument firmware may avoid this saturation and enable valid measurements at shorter ranges.

To estimate the average noise level of the transducer, we calculate burst-averaged Pr values at large ranges at low sea states at which the measured signal, not compensated for range and attenuation, does not vary with depth. At these ranges, we assume that, due to transmission losses and the weak scattering in the water column, the system is simply measuring its own electrical noise and that increases in S_v are driven primarily by the addition of the time-varying gain components in Eq. 5. This approach is consistent with those often applied in fisheries acoustics applications [*e.g.*, *De Robertis and Higginbottom*, 2007]. In our analysis, we found an average noise level of approximately 22 dB and set $Nt = 26$ dB, *i.e.*, only echogram data values with $Pr > Nt$ are considered for the bubble statistics analysis. We note that future firmware revisions and variations in internal processing parameters may result in different noise thresholds and calibration gains.

To estimate the local penetration depth of entrained bubbles, we first need to identify a threshold S_v^{th} below which the backscatter signal indicates the absence of signals associated with entrained bubbles exceeding the background conditions. These background conditions may be driven by populations of residual bubbles or biological backscattering in the upper water column. Note that the mixed layer depth was always greater than 40 m in areas sampled during the PAPA cruise; thus, acoustic scattering from stratification or turbulent microstructure can be neglected.

The local penetration depth of entrained bubbles is then defined relative to the instantaneous free surface level ($z_w = 0$) at the vertical level Z_b, in the surface-following reference frame, at which $S_v > S_v^{th}$ for $z_w \leq Z_b$; otherwise $Z_b = $ NaN (Not-a-Number). We note that this thresholding technique to estimate bubble penetration depth is analogous to the pixel intensity thresholding commonly used for whitecap coverage estimations (see §2.4). Similar thresholding techniques have been used by previous studies [*Thorpe*, 1986; *Dahl and Jessup*, 1995; *Trevorrow*, 2003; *Vagle et al.*, 2010; *Wang et al.*, 2016] with empirical S_v^{th} values ranging from -70 dB re m^{-1} to -50 dB re m^{-1} using sonars with operating frequencies ranging between $\approx$ 20 kHz and $\approx$ 200 kHz. Hereafter, we refer to this bubble detection method as BDM1.

We identified the time between 18:00 and 19:00 UTC on Dec 16 as a period with relatively calm sea surface conditions and minimal whitecapping during which no visible bubbles and surface foam were observed in the above-surface and subsurface images collected by the cameras integrated on SWIFT buoys, as well as in the images from the shipboard cameras. Furthermore, Figure 1b shows that the wind speeds just before the deployment of the SWIFTs on Dec 16 were less than 3 m s^{-1} for several hours. Figure 1b also shows that although the wind speed was increasing during the rest of the day in the presence of steady
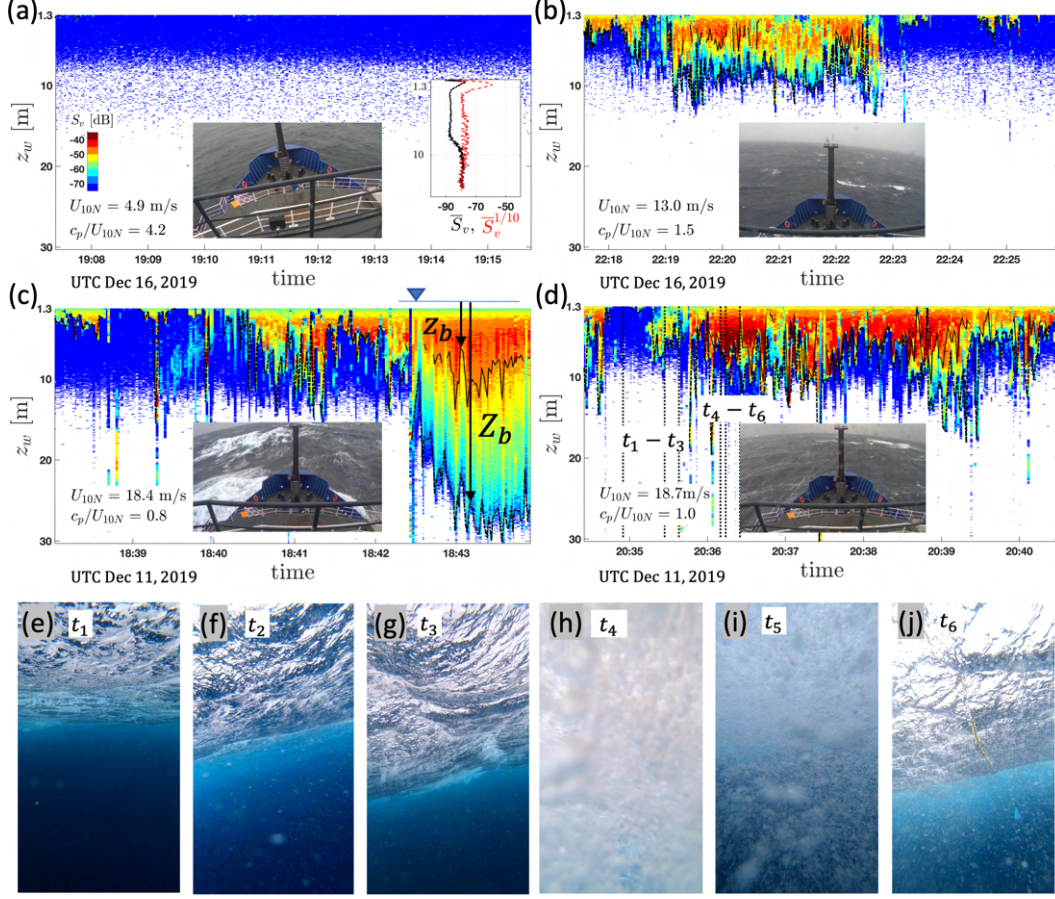
Figure 3: Examples of a depth-time map (echogram) of the volume backscattering strength S_v [dB] in ($a-b$) a rapidly evolving sea with different sea state conditions (but steady rain) on UTC Dec 16 and in ($c-d$) a storm with sustained wind speeds of $U_{10N} > 18.0\,\mathrm{m\,s^{-1}}$ on UTC Dec 11. In (a), the signal represents observations just after a steady calm sea state with minimum whitecapping and is expected to be mainly from scattering particles or bubbles not associated with breaking waves. The subsurface optical images in ($e-j$) correspond to the time instants t_1-t_6 marked by the vertical dashed lines in (d) and are collected by a GoPro camera mounted on the SWIFT buoy. Above-surface optical images in ($a-d$), taken from a camera on the ship's bridge, show a snapshot of the surface wave field within the time range of the corresponding echogram. Dotted-dashed and solid contours indicate Z_b and z_b, the two estimates of the local penetration depth of entrained bubbles defined in § 2.5. Echograms are collected by a downward-looking echosounder integrated on SWIFT buoys in a surface-following reference frame z_w, where z_w is positive downward, and $z_w=0$ represents the instantaneous free surface level.

rain, it remained below 5 m s^{-1} between 18:00 and 19:00 UTC. These observations suggest that this is a suitable period for establishing baseline levels for near-surface backscattering, with negligible contributions of bubbles injected by active breaking at the surface.

The baseline can be established by using statistical averages of the S_v from this relatively calm period with low levels of observed volume backscattering. Figure 3a shows an example echogram, above-surface image, and vertical profiles of burst-averaged and top 10%-averaged of S_v values just after the low backscattering conditions on Dec 16, as described above. The echogram data during low-backscattering conditions reveals that significant portions of the corresponding S_v values vary between -90 dB re m^{-1} and -75 dB re m^{-1}, with the burst-averaged values, $\overline{S}_v$, less than -80 dB re m^{-1}. We also found that $\overline{S}_v < -80$ dB re m^{-1} holds for the rest of calm sea state conditions ($U_{10N} < 3$ m s^{-1}, $dU_{10N}/dt < 1$ m s^{-1} / hr) within the PAPA data. We take $S_v^{th} = -70$ dB re m^{-1} (as in *Vagle et al.* [2010]) to distinguish between regions with and without the presence of recently entrained bubbles in the water column.

Even very low bubble void fractions, $O(10^{-7})$ or less, can result in S_v values greater than S_v^{th} due to the relatively strong acoustic backscattering response of bubbles [*Dahl and Jessup*, 1995; *Czerski et al.*, 2022a], even when they are sampled well above resonance. For reference, at 1 MHz, bubble radii from approximately 3 μm to 7 μm would be resonant in the upper water column [*Medwin and Clay*, 1998; *Vagle and Farmer*, 1998]. Thus, the measured backscattering reflects backscattering from an unknown and evolving population of bubbles that are slowly transported by their own buoyancy and/or local currents and turbulence.

We define another estimate of the local penetration depth of entrained bubbles as the depth $z_b (\leq Z_b)$ at which $S_v > S_v^{th}$ for $z_w \leq z_b$ and $S_v > S_v^{th} + 20$ dB for $z_b/2 \leq z_w \leq z_b$; otherwise $z_b = $ NaN. In this definition, the penetration depth is defined by the depth at which the volume backscattering signal continuously exceeds the specified threshold at the surface, and S_v values deeper in the water column exceed background thresholds by at least 20 dB. Hereafter, we refer to this bubble detection method as BDM2.

Figure 3 shows examples of echogram data and the corresponding Z_b (obtained from BDM1, dotted-dashed lines) and z_b (obtained from BDM2, solid lines) values during a developing sea on Dec 16 just after the relatively bubble-free condition described above (panels *a* and *b*) and during a storm with sustained wind speeds of greater than 18 m s^{-1} on Dec 11 (panels *c* and *d*). Additionally, Figure 3 shows examples of subsurface optical images, collected at times when $S_v < S_v^{th}$ for 1.3 m $\leq z_w$ (panel *e*), portions of S_v values are greater than S_v^{th} but remain below $S_v^{th} + 20$ dB (panels *f* and *g*), and a portion of S_v values is greater than $S_v > S_v^{th} + 20$ (panels *h*, *i* and *j*). These images qualitatively demonstrate that the entrained surface bubbles at times at which both BDM1 and BDM2 are satisfied, *i.e.*, $Z_b \neq$ NaN and $z_b \neq$ NaN, have significantly more subsurface visible optical signature than those at times at which $Z_b \neq$ NaN but $z_b = $ NaN. Comparing all available concurrent subsurface images and echogram data, we conclude that a similar trend exists across all the PAPA data.

Although we cannot ultimately constrain the differences in void fractions or bubble populations using our sampling method, we can confidently state that our second bubble detection criterion (BDM2) laid out above identifies periods during which void fractions increase by a minimum of two orders of magnitude compared to the first bubble detection criterion (BDM1). Under the simplest conditions where the bubble size distribution remains constant, a 20 dB increase in backscattering would correspond to a void fraction increase of over two orders of magnitude. This is driven by a linear relationship between backscattering and the number of scatterers as long as the distribution remains unchanged or is not attenuated by high bubble volumes (Eq. 5). Furthermore, the high bubble void fractions following breaking waves may result in significant excess attenuation of the signals, which is not accounted for in our analysis here [*Vagle and Farmer*, 1998; *Deane et al.*, 2016; *Bassett and Lavery*, 2021]. Such observations have been reported at lower frequencies, where extinction cross-sections for resonant bubbles are much larger. However, we expect that the high void

fractions following a breaking event will also have a temporary impact on measured acoustic backscatter. As a result, increases in volume backscattering following localized breaking events likely understate the increase in scattering that would otherwise be observed from the bubble populations, given the transducer's location near the surface.

In general, z_b values represent the local penetration depths of entrained bubbles with notably higher void fraction and visible optical signature than those reaching Z_b. This aligns with a broad range of prior observations measuring bubbles in the upper ocean, which consistently show significant decreases in bubble densities with increasing depth [*Vagle and Farmer*, 1998; *Medwin*, 1977b].

2.6 Defining Plume Penetration Depth and Residence Time

We define the mean, $\overline{D}_{bp}$ and $\overline{D}_{bp,v}$, and significant bubble plume depths, $D_{bp}^{1/3}$ and $D_{bp,v}^{1/3}$, as

$$\overline{D}_{bp} = \frac{\sum_{i=1}^{N_{Z_b}} Z_b^i}{N_{Z_b}}, \quad \overline{D}_{bp,v} = \frac{\sum_{i=1}^{N_{z_b}} z_b^i}{N_{z_b}}, \tag{6}$$

and

$$D_{bp}^{1/3} = \frac{\sum_{i=2N_{Z_b}/3}^{N_{Z_b}} Z_b^i}{N_{Z_b}/3}, \quad D_{bp,v}^{1/3} = \frac{\sum_{i=2N_{z_b}/3}^{N_{z_b}} z_b^i}{N_{z_b}/3}, \tag{7}$$

where $1.3 \text{ m} \leq Z_b^i \leq Z_b^{i+1} \leq 30.3 \text{ m}$, $1.3 \text{ m} \leq z_b^i \leq z_b^{i+1} \leq 30.3 \text{ m}$ (see Figure 3), and N_{Z_b} and N_{z_b} are the total numbers of the estimated Z_b (obtained from BDM1) and z_b (obtained from BDM2) values over available concurrent (1 to 4) bursts (each burst includes more than 8 minutes of data) of echogram data, respectively.

Next, we define the residence time of bubble plumes, T_{bp} and $T_{bp,v}$, as an average of the highest one-third of the apparent residence time of bubble clouds, T_b and t_b, detected in all concurrent bursts of the echogram data, given by

$$T_{bp} = \frac{\sum_{i=2N_{T_b}/3}^{N_{T_b}} T_b^i}{N_{T_b}/3}, \quad T_{bp,v} = \frac{\sum_{i=2N_{t_b}/3}^{N_{t_b}} t_b^i}{N_{t_b}/3}, \tag{8}$$

where T_b and t_b represent the residence time of bubble clouds detected by BDM1 and BDM2, respectively, with $2 \text{ s} \leq T_b^i \leq T_b^{i+1} \leq 512 \text{ s}$, $2 \text{ s} \leq t_b^i \leq t_b^{i+1} \leq 512 \text{ s}$, and N_{T_b} and N_{t_b} being the total numbers of bubble clouds detected over the available concurrent (1 to 4) bursts.

These representative bubble plume residence times, as well as mean and significant bubble plume depths, are obtained at 12-minute intervals coinciding with the availability of the wind and wave statistics. Hereafter the statistics of bubble plumes obtained from the bubble detection methods BDM1 and BDM2 (described in §2.5) are denoted by $()_{bp}$ and $()_{bp,v}$, respectively.

3 Results

In this section, we present observations of the residence time (§3.1) and the penetration depth (§3.2) of bubble plumes as well as whitecap coverage (§3.3) as a function of various wind and sea state parameters defined in §2. Estimations of the volume of bubble plumes based on the measured whitecap coverage and plume penetration depths are discussed in the next section.

3.1 Bubble Plume Residence Time

Figure 4a shows a schematic of a SWIFT track drifting through an intermittent field of saturated (with visible optical surface signature) and diffused (without visible optical surface
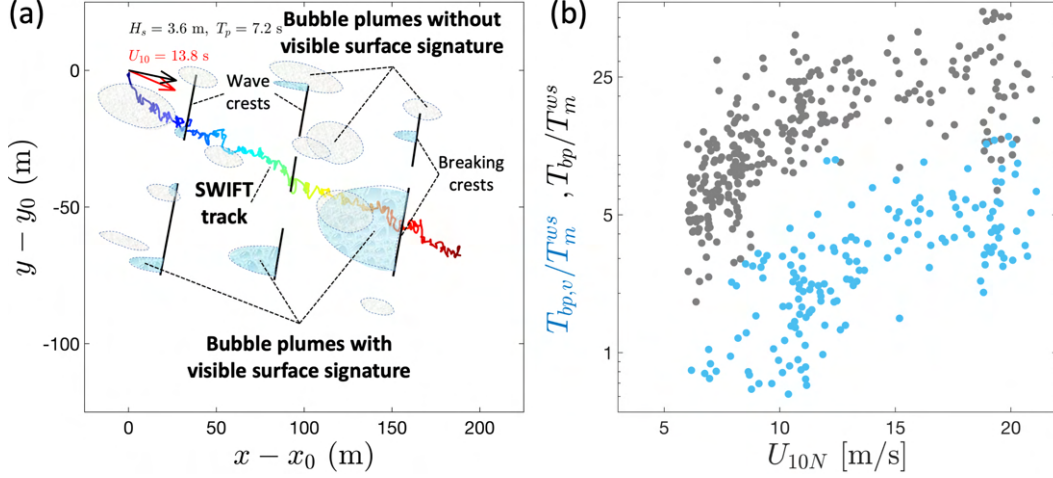
Figure 4: (*a*) Schematic of a SWIFT track (with respect to the earth frame) drifting through an intermittent field of bubble clouds during a 512-s burst, along which echogram data are collected in a surface-following reference frame, and (*b*) apparent residence time of bubble plumes in echogram data against wind speeds. In (*a*), (x_0, y_0) is the initial horizontal location of the buoy, and the black and red arrows show the dominant wave and wind directions, respectively. Subscripts bp and bp, v denote the statistics corresponding to the bubble plumes obtained from the thresholding methods BDM1 and BDM2 (described in §2.5), respectively.

signature) bubble clouds during a 512-s burst of data along which echogram data are collected in a surface-following reference frame. The buoy has a "wind slip" velocity relative to the surface water $U_{slip} \approx 0.01 U_{10N}$ that is caused by wind drag on the portion of the buoy above the surface [*Iyer et al.*, 2022]. Note that the example SWIFT track shown here is calculated with respect to the earth frame, so the example includes both the true surface current and the wind slip of the buoy (which combine together to make the observed drift velocity of the buoy, typically $U_{drift} \approx 0.04 U_{10N}$). Thus, the apparent residence time of detectable bubble clouds (defined in section 2.6) in echogram data could be shorter than their true residence time due to the relative drift of the buoys. We also note that the apparent residence time of each bubble cloud in echogram data is directly related to the way the buoy crosses the bubble cloud with respect to its main axis, as visually illustrated in Figure 4a.

Figure 4b shows the variation of the bubble plume residence times T_{bp} and $T_{bp,v}$ scaled by the wind sea mean wave period T_m^{ws} (defined in §2.3) for wind speeds greater than 6 m s^{-1}. Results indicate that the bubble plumes, especially those detected by BDM1, persist in the water column much longer than the corresponding dominant active breaking period, which is expected to be a fraction of T_m^{ws}.

Figure 5 shows the subsurface visible signature of an example evolving bubble plume at several instances during (panels (*a*1) to (*a*3)) and after (panels (*a*4) to (*a*8)) active breaking, collected by a GoPro camera on a SWIFT buoy looking from behind (upwave) the breaking event in an old sea with moderate wind speeds of $U_{10N} \approx 11$ m s^{-1} and $T_m^{ws} \approx 6$s. Figure 6 also shows example subsurface images of two evolving bubble plumes during (panels (*a* − *c*) and (*e* − *f*)) and after (panels *d* and *g* − *h*) active breaking during a storm with sustained wind speeds of $U_{10N} > 18$ m s^{-1} and $T_m^{ws} \approx 10$s. These images qualitatively show that void fractions in the bubble plumes rapidly decrease after the active breaking period and that residual void fractions persist for many wave periods. These observations are consistent with previous experimental [*Lamarre and Melville*, 1991; *Blenkinsopp and Chaplin*, 2007; *Anguelova and Huq*, 2012] and numerical [*Derakhti and Kirby*, 2014, 2016; *Derakhti et al.*,
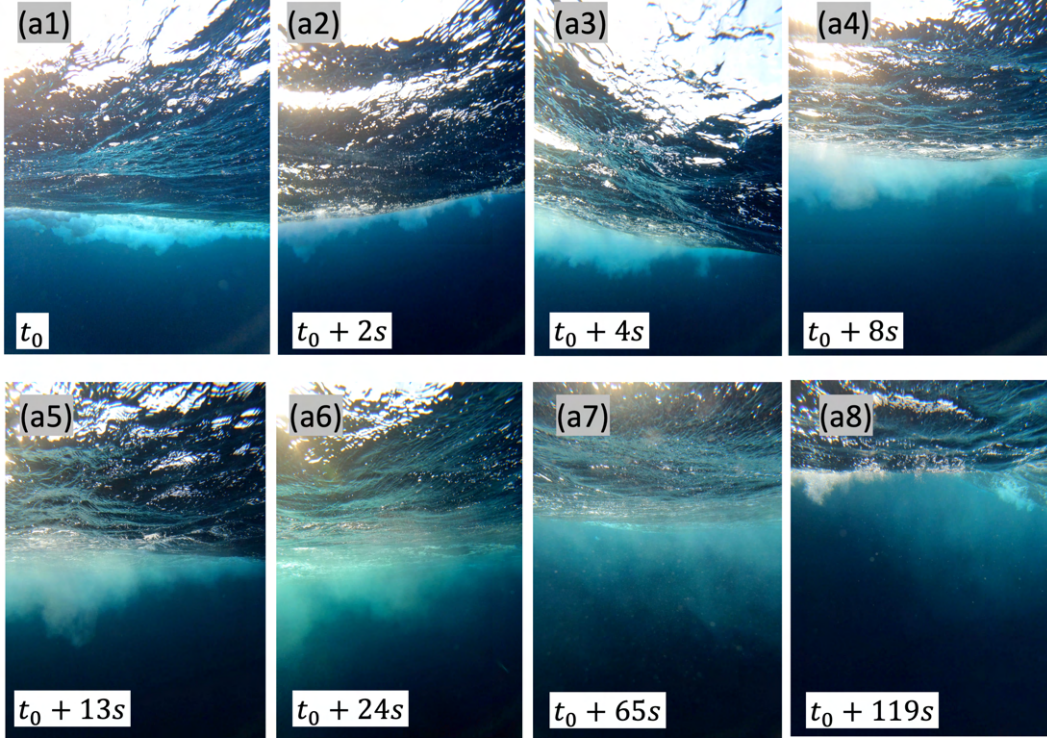
Figure 5: Example subsurface images collected by a GoPro camera on a SWIFT buoy showing the subsurface visible signature of an evolving bubble plume in an old sea with moderate wind speeds of $U_{10N} \approx 11 \text{ m s}^{-1}$.

2018, 2020a,b] studies of laboratory-scale breaking waves showing that average void fractions within bubble clouds vary from $O(10\%)$ to $O(1\%)$ during active breaking, and then drop rapidly by several orders of magnitude within a few wave periods.

As discussed in detail in §2.5, plume regions with tiny bubble void fractions, e.g., the diffused bubble clouds shown in panels $(a7)$ and $(a8)$ of Figure 5, are still detectable in our sampling method. Assuming that the scattering is dominated by bubbles with radii less than $100 \, \mu m$, the low bubble rise velocities (*i.e.*, a few cm s^{-1} or less) would yield bubble residence times of $O(\text{minutes})$ which is consistent with the apparent residence time of the bubble plumes detected by BDM1 (Figure 4b), here $T_{bp} \approx 100s$ and $\approx 200s$ for sea states similar to Figure 5 and Figure 6, respectively. Thus, the statistics of the bubble plumes detected by BDM1, referred to by subscript bp, correspond to bubble plumes ranging from saturated plumes during active breaking to highly diffused plumes that may remain in the water column long after active breaking (e.g., panel $(a8)$ of Figure 5). These observations also confirm that the bubble plumes detected by BDM2 in a given sea state represent plumes that have much shorter residence times and much more visible optical signature than those detected by BDM1 but noticeably exceed the persistence of visible surface foam formed during breaking, where $T_{bp,v} \approx 12s$ and $\approx 40s$ for sea states similar to Figure 5 and Figure 6, respectively.

3.2 Bubble Plume Penetration Depth

Example subsurface images of the bubble plume shown in Figure 5 illustrate that the average plume penetration depth (and volume) rapidly increases during the initial phase of the bubble plume evolution (e.g., panels $(a1)$ to $(a5)$, over several seconds). As shown in
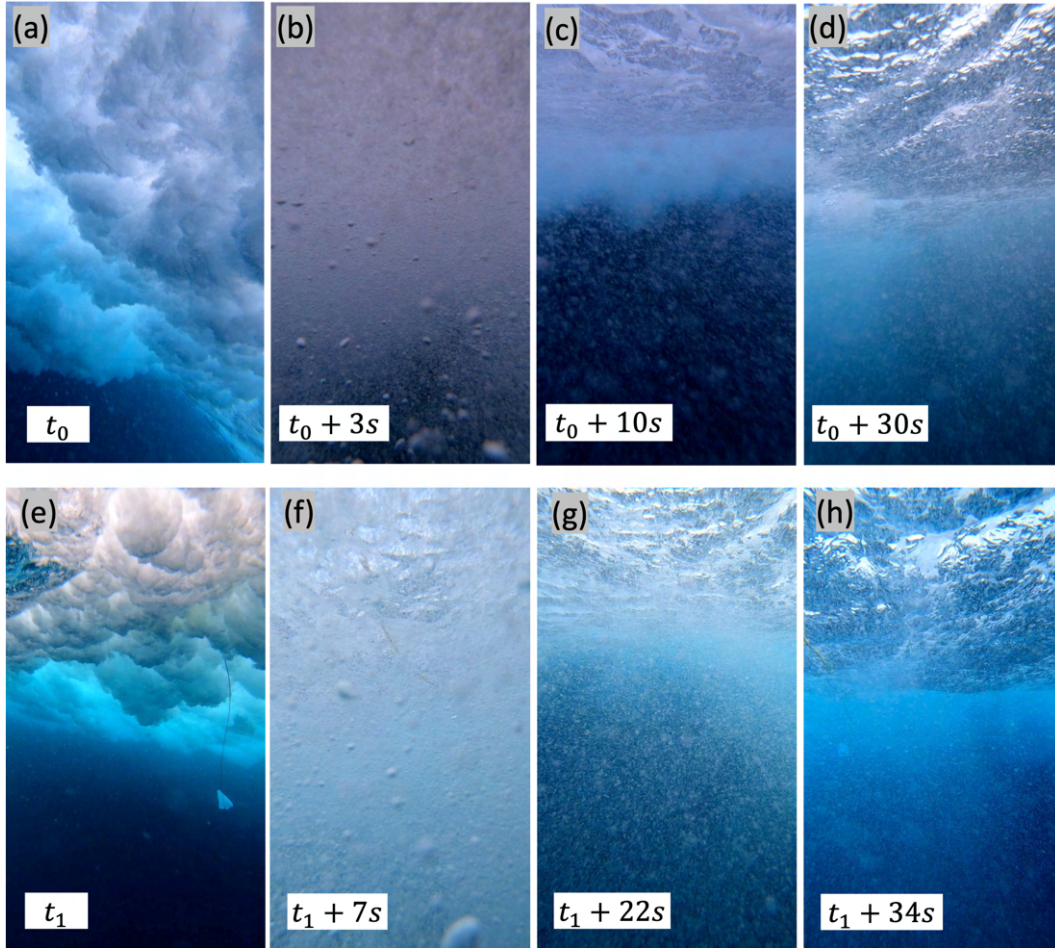
Figure 6: Example subsurface images collected by a GoPro camera on a SWIFT buoy showing the subsurface visible signature of two different evolving bubble plumes in a storm with sustained wind speeds of $U_{10N} > 18$ m s^{-1}.

panels ($a6$) to ($a8$), the overall size of the plume keeps increasing for several wave periods but at rates much lower than during active breaking. This is consistent with the evolution of bubble plumes, turbulent kinetic energy (TKE), and dye patches in previous numerical and experimental studies of laboratory-scale isolated breaking focused waves [*Rapp and Melville*, 1990; *Melville et al.*, 2002; *Derakhti and Kirby*, 2014; *Derakhti et al.*, 2018, 2020a]. Large-scale coherent structures generated by wave breaking crests are among potential drivers of such slow but persistent transport of bubbles long after active breaking [*Melville et al.*, 2002; *Derakhti and Kirby*, 2014; *Derakhti et al.*, 2016].

Figure 7 presents the variations in the mean (Eq. 6) and significant (Eq. 7) bubble plume depths as functions of wind speed U_{10N} and equilibrium range $mss/\Delta f$ (Eq. 2), along with the corresponding best fits. All the plume depth measures show strong correlations with wind speed and $mss/\Delta f$, exhibiting data scatter smaller than existing whitecap coverage datasets, including the PAPA dataset shown in Figure 11 below. Because time-dependent bubble depths less than 1.3 m are unavailable here, the resultant plume depth statistics are expected to be biased high in low winds. Hereafter, the data points with $U_{10N} < 6$ m s^{-1} are not considered in obtaining the relevant fits and their statistics (This is also a typical minimum wind speed for visible whitecaps to occur.).

Of the bubble depths defined here (by Eqs. 6 and 7 above), $\overline{D}_{bp}$ is defined similar to previous studies [*Vagle et al.*, 2010; *Wang et al.*, 2016; *Strand et al.*, 2020]. Our observations, as shown in Figure 7a, indicate that the mean bubble plume depth $\overline{D}_{bp}$ could be as high as to 14 m at $U_{10N} \approx 20$ m s^{-1}. This is in good agreement with the observations of *Vagle et al.* [2010] and *Strand et al.* [2020].

The black solid line in Figure 7a represents the best fit to the binned $\overline{D}_{bp}$ values with a power law form given by

$$\overline{D}_{bp} = 0.092 \, [U_{10N}]^{1.58} \tag{9}$$

with $r^2 = 0.90$ defined as in Eq. 13 below. As shown in Figure 7a, the linear fit by *Vagle et al.* [2010] also well describes the observed variability of $\overline{D}_{bp}$ for moderate winds. However, for high winds, the relationship between $\overline{D}_{bp}$ and wind speed becomes nonlinear, and the $\overline{D}_{bp}$ values are, on average, greater than those reported by *Vagle et al.* [2010]. This underprediction of $\overline{D}_{bp}$ at high winds in *Vagle et al.* [2010] could be simply due to the linear extrapolation of S_v at depths greater than 8 m (see their Figure 3). Additionally, *Wang et al.* [2016] also found a nonlinear relationship between mean bubble depth and wind speed at high winds. However, their mean bubble depths are significantly higher (a factor of 1.5-2) than the present (and other) observations. We note that the averaging time used to obtain $\overline{D}_{bp}$ at high winds is 8 or 16 minutes (depending on available concurrent bursts), which is comparable to that in *Wang et al.* [2016].

At any given wind speed, individual breaking events could generate bubble clouds with penetration depths much higher than $\overline{D}_{bp}$. For example, Figure 3c documents an example individual bubble cloud with a penetration depth of ≈ 30 m, which is approximately three times greater than the corresponding average bubble plume depth (*e.g.*, Eq. 9). Figure 8 illustrates that the Rayleigh distribution could reasonably describe the observed probability distribution function (PDF) of the D_{bp} values at various wind speeds, especially for $D_{bp} > \overline{D}_{bp}$. Assuming the Rayleigh distribution for D_{bp}, we obtain the significant bubble depth as $D_{bp}^{1/3} \approx 1.6\overline{D}_{bp}$, which is consistent with our observations, especially for $U_{10N} > 10$ m s^{-1}. The best fit to the observed binned $D_{bp}^{1/3}$ values with a power law form (black solid line in Figure 7c) is obtained as

$$D_{bp}^{1/3} = 0.13[U_{10N}]^{1.63}, \tag{10}$$

with $r^2 = 0.92$. Additionally, assuming the Rayleigh distribution for D_{bp}, the maximum bubble depth can be further approximated as

$$D_{bp}^{max} \approx 2D_{bp}^{1/3} \approx 3.2\overline{D}_{bp}. \tag{11}$$
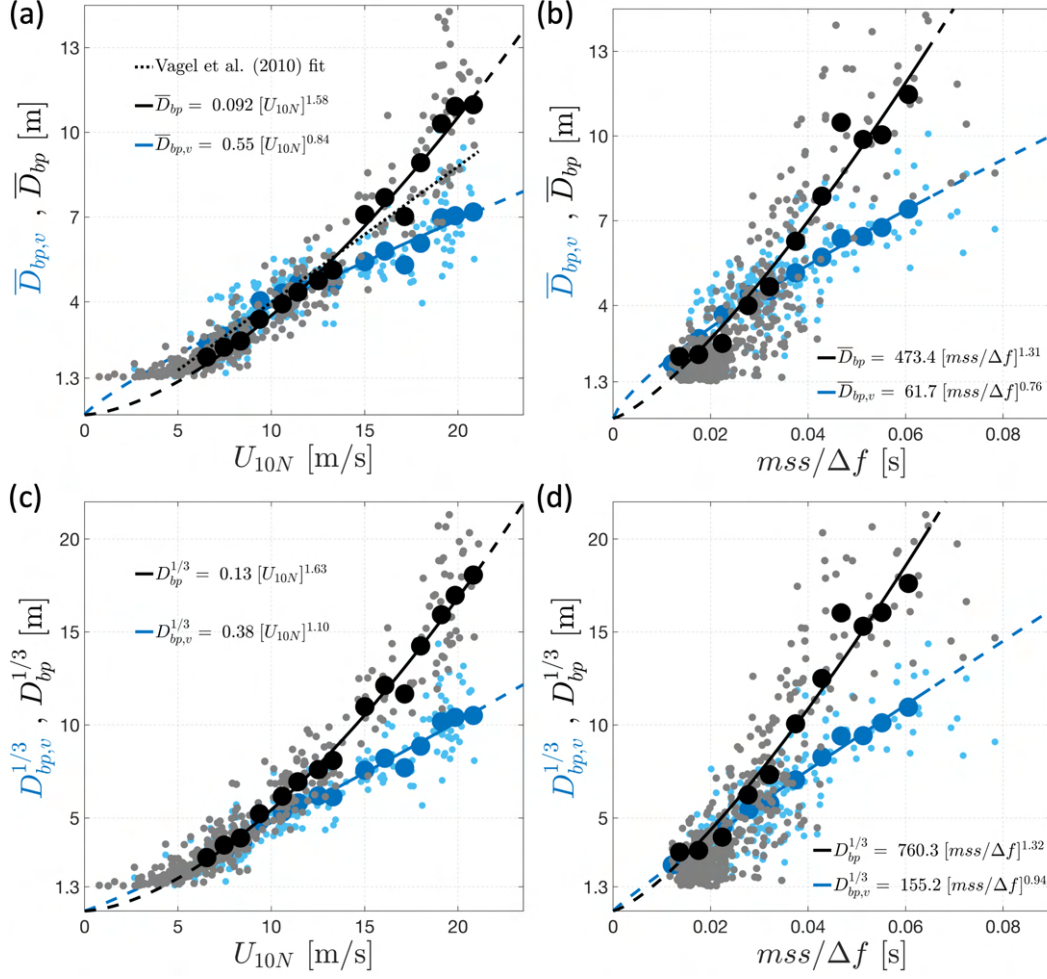
Figure 7: Observed range of ($a - b$) mean (Eq. 6) and ($c - d$) significant (Eq. 7) bubble plume depths against wind speed U_{10N} and the equilibrium range $mss/\Delta f$. Fits are obtained from the least squares fitting to the binned data points (large circles). Subscripts bp and bp, v denote the statistics corresponding to the bubble plumes obtained from the thresholding methods BDM1 and BDM2 (described in §2.5), respectively.

As explained in detail in §2.5 and consistent with observations shown in §3.1, at a given sea state condition, $D_{bp,v}$ represents the penetration depth of bubbles that have, on average, at least two orders of magnitude more void fraction and significantly more visible optical signature than those reaching D_{bp}. Figure 8 shows that the population of the bubble plume depth $D_{bp,v}$ values around their mean is considerably elevated compared to that in D_{bp}, and that the observed PDF of $D_{bp,v}$ is better described by the Gamma distribution. Furthermore, our observations show that $D_{bp,v}^{1/3}/\overline{D}_{bp,v}$ varies, on average, from 1.2 at low winds to 1.5 at high winds and that, in contrast to $D_{bp}^{1/3}$, $D_{bp,v}^{1/3}$ has an approximately linear relationship with wind speed, as shown in Figure 7. Additionally, they indicate that the ratio $D_{bp,v}^{1/3}/D_{bp}^{1/3}$ decreases with increasing wind speeds, varying from ≈ 1 at low winds to ≈ 0.6 at high winds.

We assess the predictive skill of several wind and wave parameters, commonly used in whitecap coverage parameterizations, for bubble plume depths $D_{bp}^{1/3}$ and $D_{bp,v}^{1/3}$. We evaluate the predictive performance of each predictor X (e.g., $U_{10N}, u_*, mss/\Delta f, S, R, \ldots$, all defined
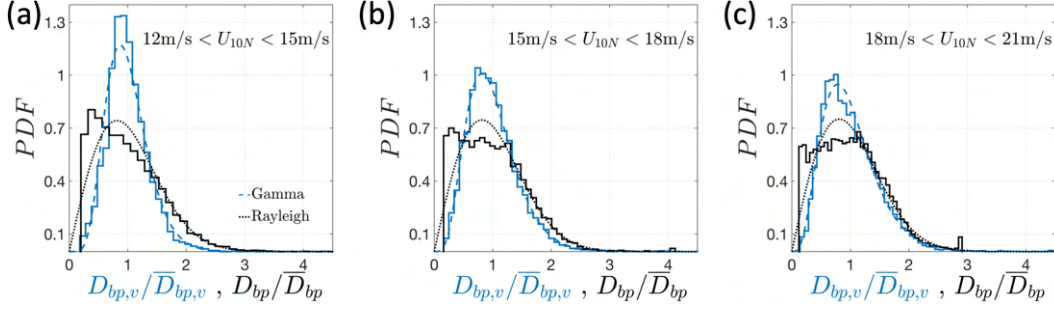
Figure 8: Probability distribution function, PDF, of the estimated bubble depths at different wind speed ranges. Dotted and dashed lines show the fitted Rayleigh and Gamma distributions to the observed PDFs.

in §2) by calculating the best fit with a power law form $a\mathcal{X}^n$ to the binned $D_{bp}^{1/3}$ and $D_{bp,v}^{1/3}$ values using the least squares method. We then compare the resulting fit statistics obtained over all individual data points with $U_{10N} \geq 6$ m s^{-1}. Bins containing fewer than four bursts of data are excluded for the data fitting process. We evaluate the overall quality of the fits using two metrics: the root-mean-square error (RMSE) and the coefficient of determination r^2, given by

$$\text{RMSE} = \sqrt{\frac{\Sigma_{i=1}^{i=N} D_{res,i}^2}{N}}, \tag{12}$$

and

$$r^2 = 1 - \frac{\Sigma_{i=1}^{i=N} D_{res,i}^2}{\Sigma_{i=1}^{i=N} (D_i - \overline{D_i})^2}, \tag{13}$$

where $D_{res,i} = D_i - [a\,(\mathcal{X}_i)^n]$, D_i represents either $D_{bp}^{1/3}$ or $D_{bp,v}^{1/3}$, N is the number of observations, and the overbar indicates an average over all the considered data points. In this context, RMSE, defined in linear space, quantifies the average deviation from the fit, while r^2 measures the proportion of the observed variability in bubble plume depths that can be predicted from the $\mathcal{X}$ parameter. A perfect fit corresponds to $RMSE \sim 0$ and $r^2 \sim 1$.

Table 1 summarizes the coefficients (a and n) and statistics (RMSE, r^2) of the best fits, $a\mathcal{X}^n$, to the PAPA data for several predictive parameters $\mathcal{X}$. Of all the parameters considered here, U_{10N} exhibits the highest skill in predicting the observed variability of both $D_{bp}^{1/3}$ and $D_{bp,v}^{1/3}$. Results summarized in Table 1 also demonstrate that the equilibrium range $mss/\Delta f$ and $H_s K_m/2$ show the highest skill among the spectral and bulk wave steepness predictors, respectively. For each type of the predictors considered here, those that contain either the peak wave height, peak wave number, or peak wave period show the least skill. These results also hold for the mean bubble plume depths statistics $\overline{D}_{bp}$ and $\overline{D}_{bp,v}$.

We now investigate the variations of scaled bubble plume penetration depths across different sea states. Our observations indicate that $D_{bp}^{1/3}$ (with the note that $\overline{D}_{bp} \approx 0.6\,D_{bp}^{1/3}$) ranges from approximately $0.4H_s$ to $4.8H_s$ and from about $0.01L_m$ to $0.20L_m$ for wind speeds exceeding 6 m s^{-1} (as shown in Figure 9), where H_s represents the significant wave height, and $L_m = 2\pi/k_m$ denotes the mean wavelength. These findings align well with the previously reported ranges of scaled mean bubble depths observed in the field [*Thorpe*, 1986; *Wang et al.*, 2016; *Strand et al.*, 2020].

Bulk wave statistics H_s and L_m (or H_p and L_p) may be completely uncorrelated with the scales of the corresponding wind sea (and dominant breaking waves) in the presence of proportionally significant swell, such as in low and moderate winds ($U_{10N} < 15$m s^{-1}) in the PAPA dataset, as illustrated in Figures 2d and 2e. Thus, we also consider the wind sea

Table 1: Parameterizations of significant bubble plume depths $D_{bp}^{1/3}$ and $D_{bp,v}^{1/3}$ represented by the best fits with a power law form $a\,\mathcal{X}^n$ as a function of several wind and wave parameters $\mathcal{X}$ to the binned PAPA data for $U_{10N} \geq 6$ m s^{-1}. The statistics of each fit are also calculated. The fits and their statistics are computed in linear space. The units for the bubble penetration depths (D_{bp}), wave heights (H), and wavelengths ($L = 2\pi/k$) are in meters [m]. The unit for Δf is in inverse seconds [1 / s]. Moreover, the units for U_{10N} and u_* are in meters per second [m / s]. The predictors of the R-, mss-, and Hk-type are all dimensionless.

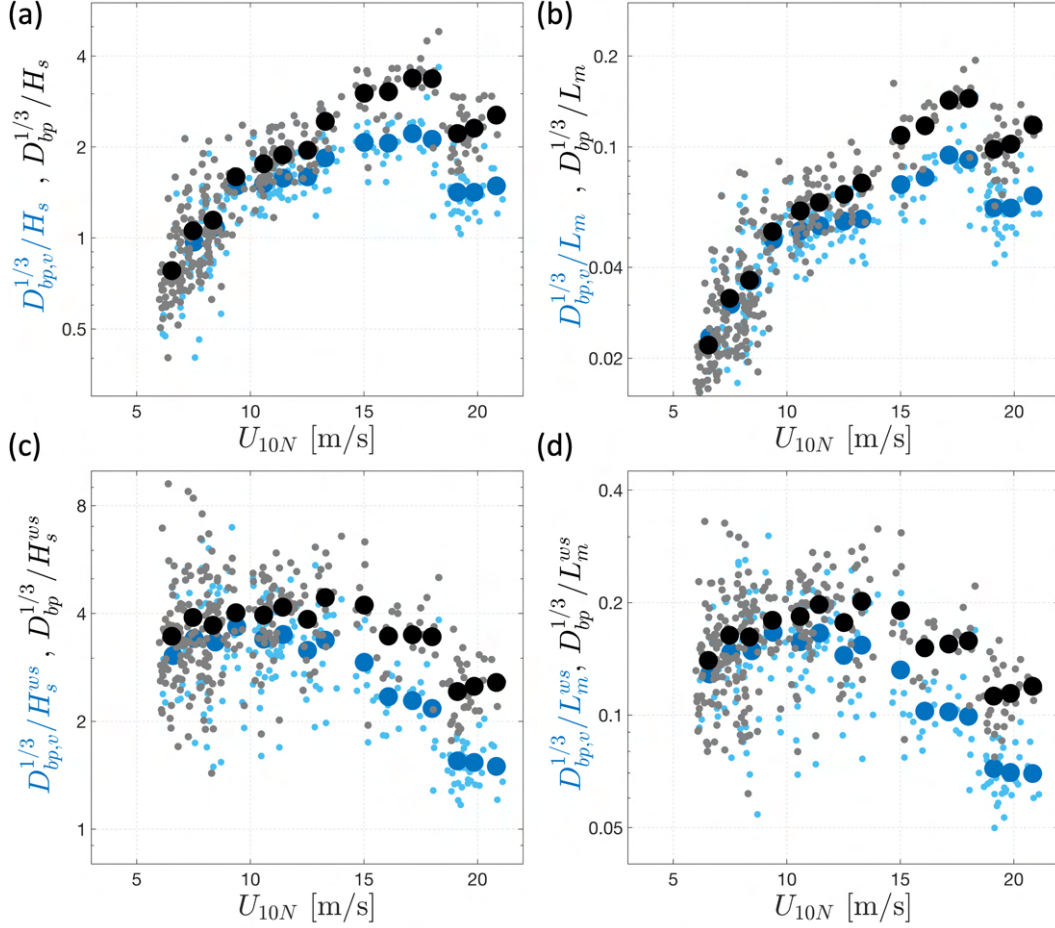| Plume Depth	Predictor $\mathcal{X}$	Results of the best fit $a\,\mathcal{X}^n$		Statistics of the best fit $U_{10N} \geq 6$ m s^{-1}	
		a	n	RMSE	r^2
$D_{bp}^{1/3}$	U_{10N}	1.27×10^{-1}	1.63	1.326	0.921
$D_{bp}^{1/3}$	u_*	1.49×10^{1}	1.14	1.417	0.910
$D_{bp}^{1/3}$	$R_{B,m} = \frac{u_*^2}{\nu_w \omega_m}$	1.07×10^{-2}	0.52	1.502	0.899
$D_{bp}^{1/3}$	$R_{B,p} = \frac{u_*^2}{\nu_w \omega_p}$	1.12×10^{-2}	0.51	1.653	0.877
$D_{bp}^{1/3}$	$R_{H_{eq}} = \frac{u_* H_{eq}}{\nu_w}$	2.56×10^{-3}	0.61	1.894	0.839
$D_{bp}^{1/3}$	$R_{H_s} = \frac{u_* H_s}{\nu_w}$	1.36×10^{-3}	0.60	1.986	0.823
$D_{bp}^{1/3}$	$R_{H_p} = \frac{u_* H_p}{\nu_w}$	2.05×10^{-3}	0.59	2.139	0.794
$D_{bp}^{1/3}$	mss	1.86×10^{4}	1.34	2.893	0.619
$D_{bp}^{1/3}$	mss$/\Delta f$	7.60×10^{2}	1.32	2.419	0.734
$D_{bp}^{1/3}$	mss$/(\Delta f \Delta \theta)$	3.35×10^{2}	1.37	2.911	0.614
$D_{bp}^{1/3}$	$H_p k_p /2$	9.06×10^{1}	0.88	4.055	0.251
$D_{bp}^{1/3}$	$H_s k_p /2$	6.33×10^{1}	0.83	4.027	0.262
$D_{bp}^{1/3}$	$H_{eq} k_m /2$	1.34×10^{4}	2.23	3.017	0.586
$D_{bp}^{1/3}$	$H_p k_m /2$	2.20×10^{3}	2.31	3.211	0.531
$D_{bp}^{1/3}$	$H_s k_m /2$	1.29×10^{3}	2.34	2.888	0.620
$D_{bp,v}^{1/3}$	U_{10N}	3.78×10^{-1}	1.10	1.112	0.822
$D_{bp,v}^{1/3}$	u_*	9.55×10^{0}	0.83	1.110	0.822
$D_{bp,v}^{1/3}$	$R_{B,m} = \frac{u_*^2}{\nu_w \omega_m}$	5.09×10^{-2}	0.38	1.139	0.813
$D_{bp,v}^{1/3}$	$R_{B,p} = \frac{u_*^2}{\nu_w \omega_p}$	4.88×10^{-2}	0.37	1.197	0.794
$D_{bp,v}^{1/3}$	$R_{H_{eq}} = \frac{u_* H_{eq}}{\nu_w}$	1.58×10^{-2}	0.45	1.290	0.760
$D_{bp,v}^{1/3}$	$R_{H_s} = \frac{u_* H_s}{\nu_w}$	9.56×10^{-3}	0.45	1.318	0.750
$D_{bp,v}^{1/3}$	$R_{H_p} = \frac{u_* H_p}{\nu_w}$	1.43×10^{-2}	0.43	1.383	0.725
$D_{bp,v}^{1/3}$	mss	1.43×10^{3}	0.94	1.917	0.466
$D_{bp,v}^{1/3}$	mss$/\Delta f$	1.55×10^{2}	0.94	1.589	0.634
$D_{bp,v}^{1/3}$	mss$/(\Delta f \Delta \theta)$	8.62×10^{1}	0.96	1.839	0.509
$D_{bp,v}^{1/3}$	$H_p k_p /2$	2.63×10^{1}	0.50	2.334	0.209
$D_{bp,v}^{1/3}$	$H_s k_p /2$	2.11×10^{1}	0.46	2.341	0.205
$D_{bp,v}^{1/3}$	$H_{eq} k_m /2$	1.25×10^{3}	1.59	1.974	0.434
$D_{bp,v}^{1/3}$	$H_p k_m /2$	2.09×10^{2}	1.44	2.000	0.419
$D_{bp,v}^{1/3}$	$H_s k_m /2$	2.15×10^{2}	1.63	1.858	0.499

Figure 9: Scaled bubble plume penetration depths against wind speeds. Here H_s is the total significant wave height, $L_m = g/2\pi * T_m^2$ is the total mean wavelength, H_s^{ws} is the wind sea significant wave height, $L_m^{ws} = g/2\pi * (T_m^{ws})^2$ is the wind sea mean wavelength, all defined in §2.3. Large circles represent the binned data points. Subscripts bp and bp,v denote statistics correspond to the bubble plumes obtained from the thresholding methods BDM1 and BDM2 (described in §2.5), respectively.

639   significant wave height H_s^{ws} and mean wavelength L_m^{ws} as scaling parameters here. Our data

640   show that $D_{bp}^{1/3}$ varies from $\approx 1.4 H_s^{ws}$ to $\approx 9.2 H_s^{ws}$ and from $\approx 0.06 L_m^{ws}$ to $\approx 0.33 L_m^{ws}$ for

641   wind speeds greater than 6 m s^{-1} (Figure 9).

642   Furthermore, the corresponding binned data indicate that $D_{bp}^{1/3}$ varies from approxi-

643   mately 2.4 to 4.4 times H_s^{ws}, and approximately from 0.11 to 0.2 times L_m^{ws} (with $\overline{D}_{bp}$ vary-

644   ing roughly from 1.6 to 2.8 times H_s^{ws}, and approximately from 0.07 to 0.13 times L_m^{ws}).

645   Interestingly, the observed range of these scaled bubble plume depths is comparable with the

646   scaled penetration depth of TKE and dye patches reported in previous numerical and experi-

647   mental studies of isolated breaking focused waves [*Rapp and Melville*, 1990; *Melville et al.*,

648   2002; *Derakhti and Kirby*, 2014; *Derakhti et al.*, 2018, 2020a], although the length scales of

649   these laboratory-scale breaking waves are one to two orders of magnitude smaller than those

650   of the dominant breaking waves in the PAPA datasets.

651   Figures 9 and 10, illustrating the dependency of scaled plume depths on wind speed

652   and wave age, reveal intriguing trends. Similar trends are observed for the other scaled plume

depths considered in our dataset. Our data reveals that all the scaled bubble plume penetration depths considered here exhibit non-monotonic variations with increasing wind speeds. However, on average, they all display decreasing trends with respect to wave age in developing seas (*i.e.*, $c_p/U_{10N} < 1.2$). In other words, during the early stages of a young sea (*i.e.*, $c_p/U_{10N} \ll 1.2$), the scaled bubble plume penetration depth, scaled by either significant wave height or mean wavelength, tends to be substantially greater (often two times or more) than in equilibrium sea states (*i.e.*, $c_p/U_{10N} \approx 1.2$). Previous field observations revealed that the former is dominated by plunging breaking waves *Thorpe* [1992], while the dominant breaker type in the latter is expected to be spilling breaking. Notably, prior numerical and experimental studies of laboratory-scale breaking waves have consistently demonstrated that bubbles (and the associated breaking-generated turbulence) penetrate, on average, deeper beneath plunging breakers compared to spilling breakers of equivalent length scales, especially during active breaking periods [*Rapp and Melville*, 1990; *Melville et al.*, 2002; *Derakhti and Kirby*, 2014; *Derakhti et al.*, 2018, 2020a,b]. Hence, the observed dependence of scaled bubble plume penetration depths on wave age in developing seas, as illustrated in Figure 10, can be attributed to the change in dominant breaker types. We note that our observed dependence of scaled bubble depth on wave age is consistent with the dependence of bubble-mediated gas flux on wave age reported by *Liang et al.* [2017].

Furthermore, our results reveal a monotonic decrease in scaled bubble plume penetration depths, scaled by either H_s or L_m, with increasing wave age across the observed range of sea states in the PAPA dataset, spanning from developing to old seas. Specifically, our data indicates that $D_{bp}^{1/3}/H_s$ has a linear relationship with the inverse of wave age, given by

$$\frac{D_{bp}^{1/3}}{H_s} = 2.42 [\frac{c_p}{U_{10N}}]^{-0.96}.$$

(14)

This relationship, shown by the solid line in Figure 10a, exhibits relatively small data scatter with $r^2 = 0.77$. Assuming an approximately linear relationship between U_{10N} and air friction velocity (Figure 2b), our findings in Figures 10a and 10b and Eq. 14 align with the corresponding results reported in *Wang et al.* [2016].

3.3 Whitecap Coverage and Its Relation with Bubble Plume Depths

Existing parameterizations of oceanic whitecap coverage W generally take a threshold power law form $W = a(\mathcal{X} - b)^n$, where $\mathcal{X}$ is a selected predictive parameter (e.g., $U_{10N}, u_*, \text{mss}/\Delta f, S, R, \ldots$, all defined in §2). The coefficients a, b, and n are empirically determined through best-fit curve fitting, minimizing the sum of the squares of the log residuals $W_{res} = \log_{10} W - \log_{10}[a(\mathcal{X} - b)^n]$. This approach ensures that equal weight is given to W data across several orders of magnitude.

It is widely recognized that various environmental factors contribute to the scatter in whitecap variability for a given predictive parameter $\mathcal{X}$. These factors may include surfactants, salinity, wind fetch and duration, wind history, surface shear, and rain. However, these secondary effects are generally thought to have a relatively minor impact on the mean values of W. Consequently, we obtain the corresponding best fits over the binned data as in §3.2 and similar to *Scanlon and Ward* [2016] and *Brumer et al.* [2017]. Bins with fewer than four bursts of data are excluded from the fitting process.

Figures 11a and 11b show the variation of whitecap coverage (W) in the PAPA dataset and the dataset of *Schwendeman and Thomson* [2015a] against wind speed (U_{10N}) and air friction velocity (u_*). The panels also include best-fit curves obtained from the binned PAPA data, as well as several relevant threshold power law fits from recent literature [*Sugihara et al.*, 2007; *Callaghan et al.*, 2008; *Schwendeman and Thomson*, 2015a; *Scanlon and Ward*, 2016; *Brumer et al.*, 2017]. Consistent with recent studies, the observed values of W as functions of U_{10N} are considerably smaller than those reported in early whitecap coverage studies [e.g., *Monahan and Muircheartaigh*, 1980], which relied on manual whitecap extraction
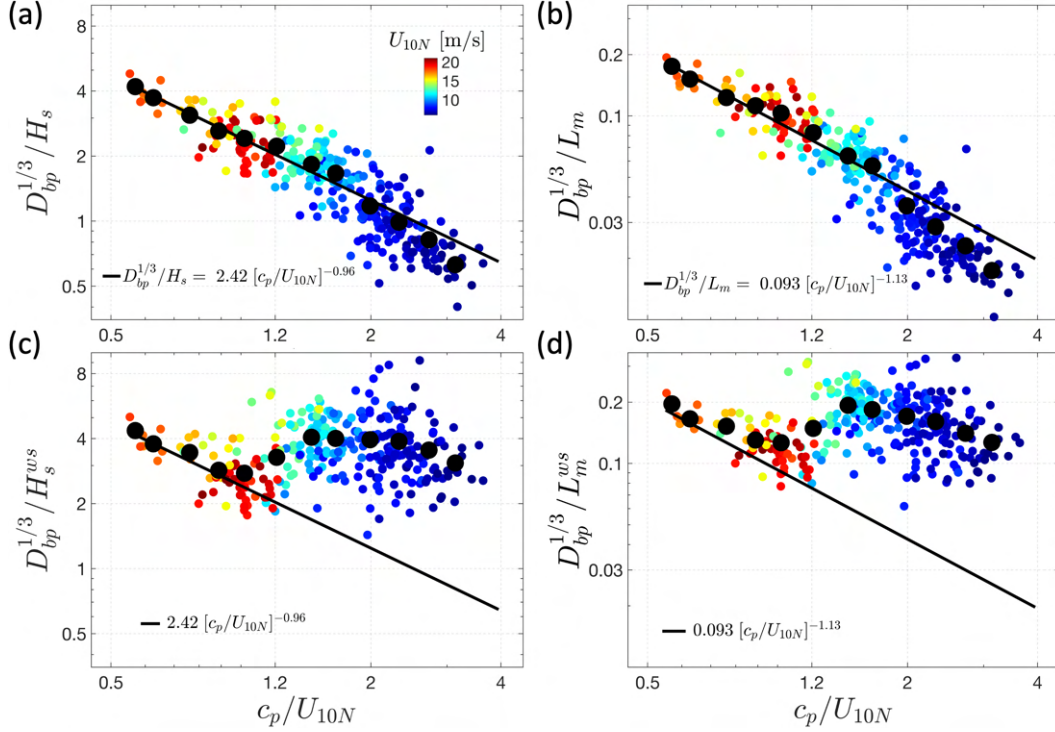
Figure 10: Scaled bubble plume depths against wave age color-coded based on the corresponding wind speeds. In (*a*) and (*b*), the fits are obtained from the least squares fitting to the binned data points (large circles). Definitions are as in Figure 9.

methods [*Monahan*, 1969]. Furthermore, the observed range of $W(U_{10N})$ and $W(u_*)$ values and their associated data scatter are consistent with recent studies that employed experimental methods comparable to those used in this study (see §2.4).

Figure 11a shows that the observed $W(U_{10N})$ values and their corresponding best fits at high winds are considerably comparable with those in the other datasets, especially those that include W observations at $U_{10N} > 16$ m s^{-1}. The solid line section of each fit shown in Figure 11 represents the range of data used to obtain the best fit. However, it is worth noting that the fits tend to diverge for $U_{10N} < 10$ m s^{-1}. This divergence can be attributed to the sensitivity of the shape of a threshold power law fit, particularly the coefficient b (which incorporates the threshold behavior of the fit), to the data at the lower range of X values. Thus, any systematic bias in the selected wind parameter at low wind speeds will impact the resulting best fit. Several previous studies did not correct wind speeds for atmospheric stability, e.g., *Sugihara et al.* [2007] and *Schwendeman and Thomson* [2015a], or they used U_{10}^{PL} as a proxy for U_{10N}, e.g., *Callaghan et al.* [2008]. As discussed in §2.2, while these simplifications have a relatively minor effect on estimated wind speeds at high winds, they can introduce significant errors in estimated wind parameters at low winds.

Our observations shown in Figures 11a and 11b illustrate that the observed $W(U_{10N})$ and $W(u_*)$ values exhibit significant variation when wind speeds are rapidly decreasing ($dU_{10N}/dt \ll 0$) and are at low levels ($U_{10N} < 4$ m s^{-1} or $u_* < 0.2$ m s^{-1}), ranging from 10^{-4} and 2×10^{-3}. In contrast, the best wind-speed-only or u_*-only fits obtained from the remaining data points predict no whitecapping ($W = 0$) at these low wind conditions. This suggests that a strong wind history may result in a systematic bias in $W(U_{10N})$ and $W(u_*)$ data at low winds, potentially contributing to the apparent divergence observed in existing wind-speed-only and u_*-only fits at low and moderate wind speeds.
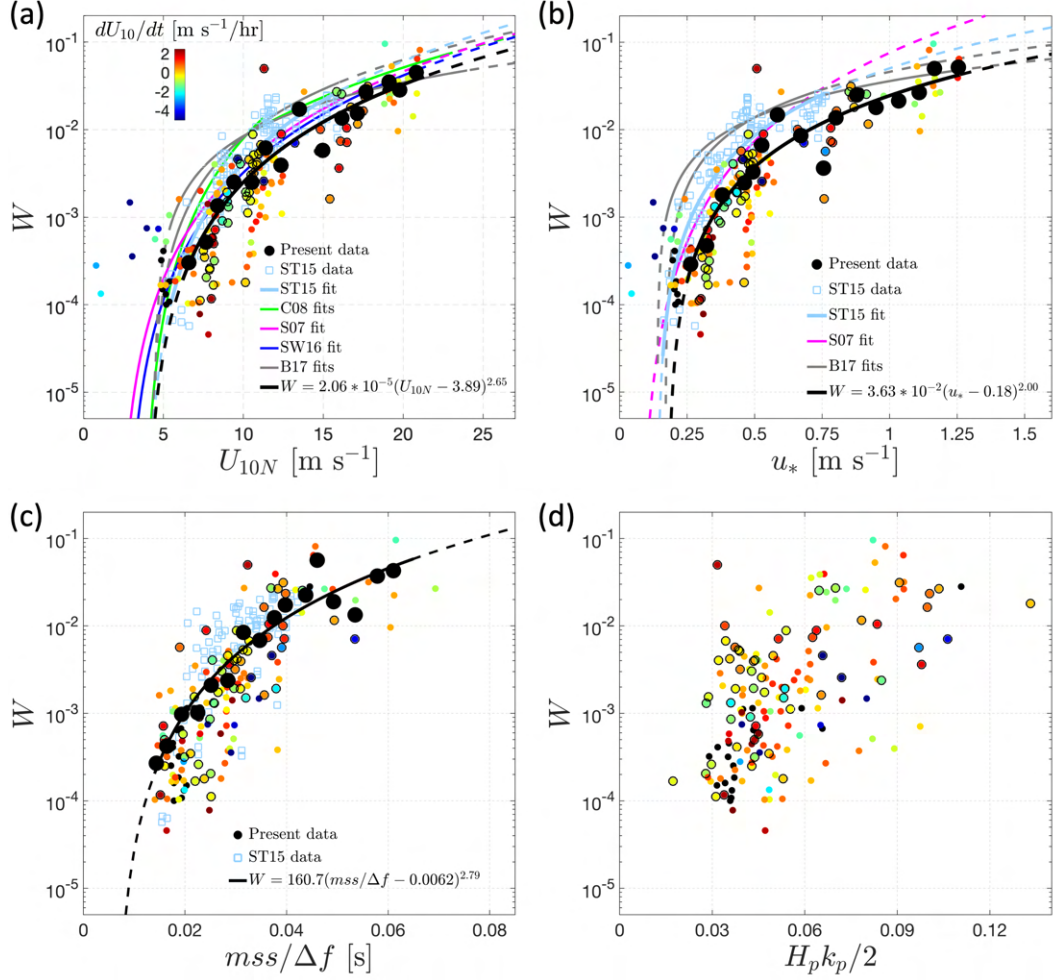
Figure 11: Observed range of whitecap coverage against various environmental factors: (*a*) wind speed U_{10N}, (*b*) air friction velocity u_*, (*c*) the equilibrium range $mss/\Delta f$, and (*d*) the significant spectral peak steepness $H_p k_p/2$ (all defined in §2). Each data point is color-coded based on the corresponding wind accelerations dU_{10N}/dt. Circles with black edges indicate observations in the presence of rain (rain rates have not been measured). The best fits to the present data are obtained from the least squares fitting to the bin-averaged data points (large black circles).

Figures 11a and 11b also present compelling evidence that, under similar wind forcing represented by either U_{10N} or u_*, a significant portion of W values in the PAPA dataset exhibit tendencies to be smaller and larger than the corresponding mean W values predicted by the best fits during increasing ($dU_{10N}/dt > 0$) and decreasing ($dU_{10N}/dt < 0$) wind speeds, respectively. This trend is consistent with the observations of *Callaghan et al.* [2008] for wind speeds exceeding approximately 9 m s^{-1}. However, in contrast to *Callaghan et al.* [2008], our observations extend this trend to encompass moderate and low winds, provided that the magnitude of dU_{10N}/dt is sufficiently large.

Next, we assess the predictive skill of several wind and wave parameters for the observed range of W values in the PAPA dataset, employing a methodology similar to that described in §3.2. However, in this analysis, we work in $\log_{10}$ space. To evaluate the overall quality of the fits, we employ Eqs. 12 and 13, with $W_{res,i} = \log_{10} W_i - \log_{10}[a (\mathcal{X}_i - b)^n]$. In this context, RMSE quantifies the average order of magnitude deviation from the fit, while r^2 measures the proportion of the observed $\log_{10} W$ variability that can be predicted from the $\mathcal{X}$ parameter. Note that a negative r^2 value indicates that the fit performs worse than a horizontal line at the mean of the data. Similar to the approach in §3.2, all the fits are obtained from the binned data for $U_{10N} \geq 6$ m s^{-1}. The fit statistics are computed using individual 10-minute average data points, W_i ($i = 1, \ldots, N$), with three conditions: including all data ($N = 165$), limiting to $U_{10N} \geq 6$ m s^{-1} ($N = 144$), and restricting to $|dU_{10N}/dt| < 2$ m s^{-1}hr^{-1} ($N = 126$).

Table 2: Parameterizations of whitecap coverage represented by the best fits with a threshold power law form $W = a (\mathcal{X} - b)^n$ as a function of several wind and wave parameters $\mathcal{X}$. These fits are obtained from the binned PAPA data for $U_{10N} \geq 6$ m s^{-1} under three specific conditions. These fits and their associated statistics are computed in log space. Throughout the paper, whitecap coverage W is presented as a dimensionless fraction. The units for wave heights (H) and wavelengths ($L = 2\pi/k$) are meters [m]. The unit for Δf is in inverse seconds [1 / s]. Moreover, the units for U_{10N} and u_* are in meters per second [m / s]. The predictors of the R-, mss-, Hk-type are all dimensionless.

| Predictor | Results of the best fit $W = a(\mathcal{X} - b)^n$ | | | Statistics of the best fit with conditions: | | | | | |
| | | | | $U_{10N} \geq 6$ m s^{-1} | | $\lvert\frac{dU_{10N}}{dt}\rvert < 2\,\frac{\text{ms}^{-1}}{\text{hr}}$ | | all data | |
$\mathcal{X}$	a	b	n	RMSE	r^2	RMSE	r^2	RMSE	r^2
U_{10N}	2.06×10^{-5}	3.89	2.65	0.412	0.70	0.471	0.60	0.752	0.05
u_*	3.63×10^{-2}	0.18	2.00	0.394	0.72	0.476	0.59	0.698	0.18
$R_{B,m} = \frac{u_*^2}{\nu_w \omega_m}$	3.87×10^{-9}	5.81×10^4	1.14	0.400	0.72	0.646	0.25	0.935	-0.47
$R_{B,p} = \frac{u_*^2}{\nu_w \omega_p}$	3.86×10^{-9}	7.01×10^4	1.12	0.424	0.68	0.657	0.22	0.916	-0.41
$R_{H_{eq}} = \frac{u_* H_{eq}}{\nu_w}$	3.02×10^{-10}	1.50×10^5	1.31	0.428	0.68	0.415	0.69	0.645	0.30
$R_{H_s} = \frac{u_* H_s}{\nu_w}$	2.45×10^{-10}	5.07×10^5	1.23	0.456	0.63	0.434	0.66	0.692	0.20
$R_{H_p} = \frac{u_* H_p}{\nu_w}$	1.64×10^{-9}	4.05×10^5	1.12	0.590	0.38	0.589	0.37	0.801	-0.08
mss	6.50×10^6	$-$	3.60	0.565	0.43	0.557	0.44	0.572	0.44
mss/Δf	1.61×10^2	6.23×10^{-3}	2.79	0.487	0.58	0.482	0.58	0.512	0.55
mss/$(\Delta f \Delta \theta)$	4.79	1.72×10^{-2}	2.16	0.537	0.49	0.534	0.49	0.557	0.47
$H_p k_p/2$	4.85	$-$	2.33	0.737	0.03	0.520	0.06	0.778	-0.04
$H_s k_p/2$	2.06×10^{-1}	3.86×10^{-2}	0.99	0.766	-0.05	0.795	-0.14	0.837	-0.20
$H_{eq} k_m/2$	1.89×10^7	$-$	6.58	0.564	0.43	0.550	0.46	0.576	0.43
$H_p k_m/2$	3.80×10^2	3.12×10^{-2}	3.87	0.547	0.46	0.550	0.46	0.552	0.48
$H_s k_m/2$	5.53×10^2	4.56×10^{-2}	4.27	0.507	0.54	0.502	0.54	0.503	0.56

Table 2 summarizes the coefficients (a, b, and n) and statistics associated with the best fits, represented as $W = a\,(X - b)^n$, for several predictive parameters X to the PAPA dataset. Among all the predictors considered for W at moderate and high wind conditions, u_* demonstrates the strongest fit ($r^2 = 0.72$, RMSE = 0.394), with only a slight advantage over the U_{10N} fit ($r^2 = 0.70$, RMSE = 0.412). Our results highlight that the fits obtained from different variations of the predictors R_H (Eq. 3) and R_B (Eq. 4), which incorporate both u_* and a characteristic scale of the wave field, exhibit comparable or slightly weaker performance than the u_*-only fit. Importantly, these parameterizations are not able to reasonably predict W under conditions of rapidly varying wind speeds, characterized by large wind accelerations.

Our observations in Figure 2 illustrate that either the normalized or unnormalized equilibrium range mss values tend to be smaller at increasing winds compared to those in decreasing winds at a given wind speed. This observation suggests that these spectral parameters may reflect a combination of wind forcing and wind history effects. In alignment with these observations, the results presented in Table 2 emphasize that the parameterizations based on the equilibrium range mss exhibit consistent skill across various sea state conditions, even in conditions with substantial wind accelerations. Specifically, the equilibrium range $mss/\Delta f$ (Figure 11c) appears to be a more reliable predictor of the observed variability in W compared to other spectral predictors considered. Among the bulk steepness predictors, $H_s k_m/2$ demonstrates the highest skill. Overall, among the predictor types explored in this analysis, those incorporating either peak wave height, peak wave number, or peak wave period appear to have the least skill (Figure 11d). Additionally, a recent study by *Malila et al.* [2022] suggests that wave field groupiness may exhibit superior predictive skill in predicting the variability of W compared to conventional bulk wave spectrum predictors.

Figure 11 shows that the observed $W(U_{10N})$, $W(u_*)$, and $W(mss/\Delta f)$ values in the PAPA dataset at moderate winds (e.g., $8\ \mathrm{m\ s^{-1}} \leq U_{10N} \leq 16\ \mathrm{m\ s^{-1}}$) are generally smaller than the *Schwendeman and Thomson* [2015a] dataset. Notably, a significant portion of the data at these wind speeds was collected in the presence of rain (Figure 1b). This observation highlights the potential influence of rain on whitecap activity, a phenomenon that has been observed by mariners for decades but has yet to be quantified. Detailed quantification of the effects of rain on W would require measurements of rain rates, which were not available in this study.

Finally, Figure 12 illustrates that the mean and significant bubble plume penetration depths are, on average, correlated and exhibit a nonlinear relationship with whitecap coverage, given by

$$\overline{D}_{bp} = 29.5\ W^{0.33}\,,\quad D_{bp}^{1/3} = 52.8\ W^{0.36}, \tag{15}$$

with $r^2 = 0.60$ (for the fit in Figure 12a) and $r^2 = 0.62$ (for the fit in Figure 12c), and

$$\overline{D}_{bp,v} = 12.6\ W^{0.19}\,,\quad D_{bp,v}^{1/3} = 21.9\ W^{0.24}, \tag{16}$$

with $r^2 = 0.33$ (for the fit in Figure 12b) and $r^2 = 0.43$ (for the fit in Figure 12d). These fits are obtained using the binned data as a function of U_{10N}, with data points corresponding to $U_{10N} < 6\mathrm{m\ s^{-1}}$ excluded from the fitting process. As detailed in §2.5 and consistent with the observations presented in §3.1 and §3.2, $D_{bp,v}$ represents the penetration depth of bubbles characterized by, on average, at least two orders of magnitude higher void fraction and significantly more visible optical signature compared to those reaching D_{bp} for a given sea state condition.

Intuitively, increasing the rate of breaking events with the same scale leads to a linear increase in W without affecting mean bubble plume depth. However, in reality, wave breaking occurs across a range of scales. Therefore, the increase in W results from both a higher rate and larger-scale breaking waves. This may partially explain the observed relationship between bubble plume depths and W shown in Figure 12. In other words, on average, plume depths tend to increase with increasing W, but at a considerably lower rate. This is reflected in the exponents in Eqs. 15 and 16, which are positive but significantly less than 1.
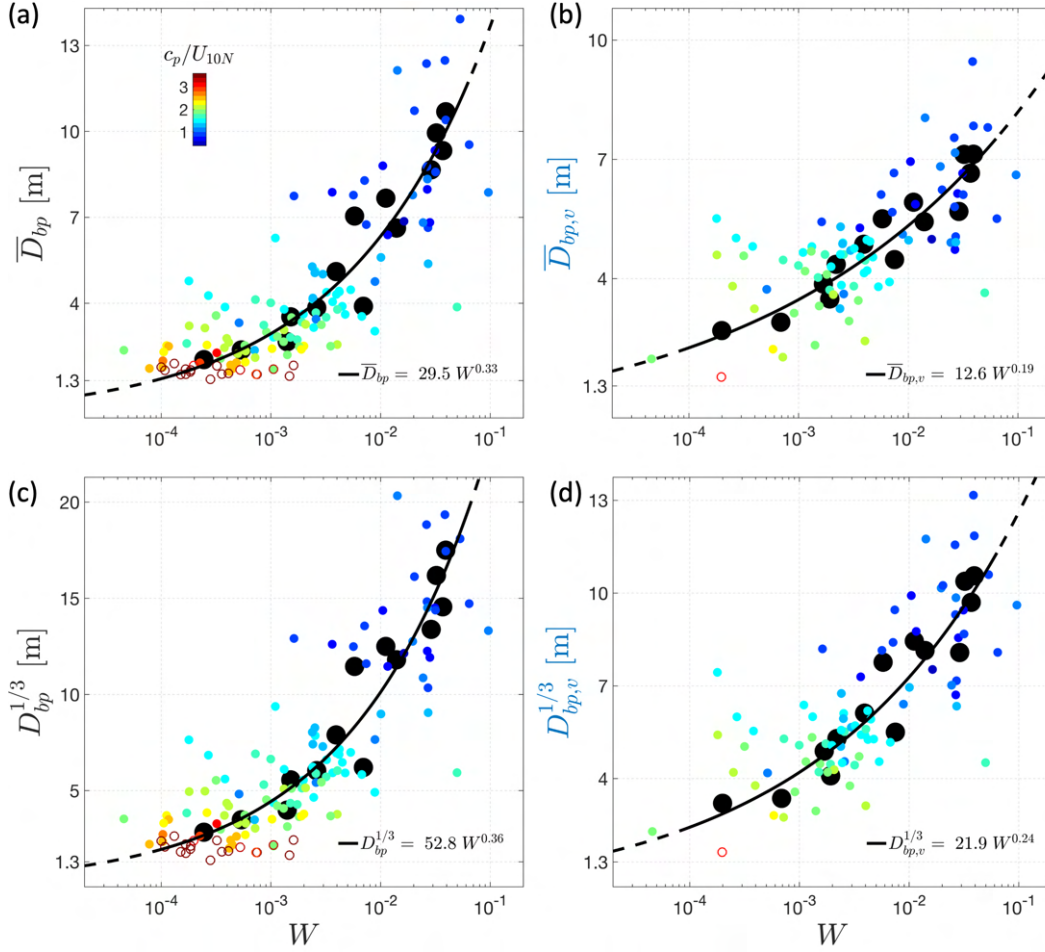
Figure 12: Mean and significant bubble plume depths against whitecap coverage. The best fits to the present data are obtained through least squares fitting to the bin-averaged data points as a function of U_{10N} (large black circles). Open circles denote the data with $U_{10N} < 6$ m s^{-1}.

4 Discussion: Bubble Plumes Volumes

In this section, we define the volume of bubble plumes as a measure of their overall size rather than the total volume of bubbles they contain. As detailed in §2.5, these bubble plumes are identified as regions where volume backscattering strength, which is somewhat related to bubble void fractions, exceeds a specific threshold value. With this definition, the volume of bubble plumes per unit sea surface area can be expressed as

$$\mathcal{V}_{bp} = \mathcal{A}_{bp}\overline{D}_{bp}, \ \ \text{and} \ \ \mathcal{V}_{bp,v} = \mathcal{A}_{bp,v}\overline{D}_{bp,v}, \tag{17}$$

where $\mathcal{A}$ represents the fractional surface area of bubble plumes, $\overline{D}$ is the mean penetration depth of bubbles within these plumes, and the subscripts bp and bp,v denote the statistics corresponding to the bubble plumes obtained using our bubble detection methods BDM1 and BDM2 (as described in §2.5), respectively. As elaborated in §2.5, $\overline{D}_{bp,v}$ represents the mean penetration depth of bubbles where the volume backscattering is at least 20 dB higher compared to $\overline{D}_{bp}$ for a given sea state condition. Note that this difference in backscattering strength is expected to reflect a significant increase in bubble void fraction. Our observations and several simple parameterizations of the mean plume depths $\overline{D}_{bp}$ and $\overline{D}_{bp,v}$ are presented in §3.

We note that $\mathcal{A}$ represents the fractional surface area, with or without a visible surface signature, of bubble plumes that persist significantly longer than the visible surface foam generated during active breaking, as discussed in §3.1. Therefore, both $\mathcal{A}_{bp}$ and $\mathcal{A}_{bp,v}$ are expected to be noticeably greater than the measured whitecap coverage W. However, our sampling method does not allow for a direct quantification of $\mathcal{A}_{bp}$ and $\mathcal{A}_{bp,v}$. In the following, we introduce a proxy for $\mathcal{A}$ and comment on its relation to W.

We define P as a time fraction of echogram data over concurrent bursts during which bubble plumes are detected. Assuming the buoys had an approximately constant "wind slip" velocity U_{slip} during each burst, $A = P^2$ then provides a proxy for $\mathcal{A}$ if the drifting distance of the buoy relative to the surface water $\approx U_{slip}T_{burst}$ is much greater than the average horizontal length of the bubble clouds $\approx U_{slip}T_{ab}$ or $U_{slip}T_{ab,v}$ (see §3.1). Further, at least a few bubble clouds should be available in a burst to consider that $\mathcal{A} \approx A$.

Figure 13a shows the A_{bp} and $A_{bp,v}$ values as a function of U_{10N} where the size of the symbols is a function of the number of the bubble clouds detected in a burst, averaged over concurrent bursts, N, with $0.67 \leq N_{bp} \leq 26$ and $0.5 \leq N_{bp,v} \leq 24$. Note that P, and thus $A = P^2$, values that approach one indicate that either the main portion of the surface layer is covered by bubble plumes or the net drifting distance of the buoy (relative to the surface water) is smaller than the horizontal length of the sampled bubble cloud. As shown in Figure 4b and 13a, the latter may explain $A_{bp} \sim 1$ at moderate winds where $N < 2$ and T_{ab} values are on the order of several hundreds of seconds (comparable to $T_{burst} = 512s$). Despite the uncertainties in the interpretation of A, the observations shown in Figure 13a suggest that A_{bp} is several times greater than $A_{bp,v}$, which is qualitatively consistent with the continuous increase of the overall size of the bubble plume shown in Figure 5 and the corresponding residence time results shown in Figure 4b.

Figure 13b shows that both A_{bp} and $A_{bp,v}$ are, on average, increase as a function of W as

$$A_{bp} = 2.5\,W^{0.33} \leq 1, \ \ \text{and} \ \ A_{bp,v} = 8.4\,W^{0.97} \leq 1. \tag{18}$$

Note that the data points with $N < 3$ are neglected in Figure 13b. Our observations show that A_{bp}, which is comparable to a fractional surface area defined in *Thorpe* [1986], is at least an order of magnitude larger than W. This is consistent with the semi-empirical plume area analysis of *Thorpe* [1986].

Finally by substituting Eqs. 15, 16, and 18 into Eq. 17, we obtain

$$\mathcal{V}_{bp} = \mathcal{A}_{bp}\overline{D}_{bp} \approx 74\,W^{0.66} \leq 29.5\,W^{0.33} \ \ [\text{m}^3/\text{m}^2], \tag{19}$$
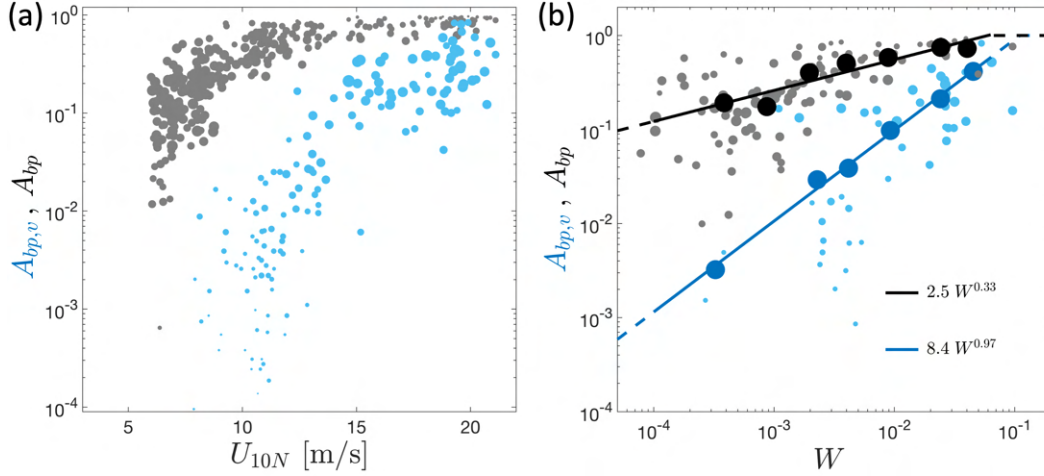
Figure 13: Proxy for the fractional area of the bubble plumes against (a) wind speed and (b) whitecap coverage. Symbol sizes are a function of the number of bubble clouds detected in a burst averaged over concurrent (1 to 4) bursts ranging from 0.5 to 26. In (b), large symbols represent the corresponding binned data with more than three detected bubble clouds in a burst. Subscripts bp and bp, v denote the statistics corresponding to the bubble plumes obtained from the thresholding methods BDM1 and BDM2 (described in §2.5), respectively.

and

$$\mathcal{V}_{bp,v} = \mathcal{A}_{bp,v}\overline{D}_{bp,v} \approx 106\,W^{1.16} \leq 12.6\,W^{0.19} \quad [\text{m}^3/\text{m}^2], \tag{20}$$

assuming that the best fits to the binned data shown in Figure 13b (Eq. 18) provide a proxy for $\mathcal{A}_{bp}$ and $\mathcal{A}_{bp,v}$.

We emphasize that uncertainty in our estimates of the fractional surface area of bubble plumes (and thus plume volumes) increases with decreasing W, especially at low W values (e.g., $W < 10^{-3}$) because of increasing effect of sparse sampling of intermittent breaking crests on the resulting statistics [*Derakhti et al.*, 2020a].

5 Summary

The observational results presented in this study quantify the statistics of penetration depth and fractional surface area of bubble plumes generated by breaking surface waves as a function of various wind and sea state parameters across a wide range of sea state conditions. Bubble plume data include concurrent high-resolution (with a 12 minutes temporal resolution) plume depth statistics and whitecap coverage. The former is obtained from the echogram data with 1 cm vertical resolution, collected by downward-looking echosounders mounted on arrays of freely drifting SWIFT buoys. The latter is obtained from visual images, collected by shipboard cameras operated near the buoys. The findings offer valuable insights into the size characteristics of bubble plumes under varying environmental conditions.

Our observations highlight strong correlations between the statistics of bubble plume penetration depths and environmental factors such as wind speed, spectral wave steepness, and whitecap coverage. Notably, we find that at high wind speeds, the mean plume depths extend beyond 10 m beneath the surface, with individual bubble clouds reaching depths exceeding 30 m.

Furthermore, our results reveal that the mean plume depths exhibit variations, on average, ranging from 1.6 to 2.8 times the wind sea significant wave height H_s^{ws}. Scaled plume depths, by either H_s^{ws} or the total significant wave height H_s, demonstrate a non-monotonic relationship with increasing wind speeds. Interestingly, plume depths scaled by H_s exhibit a robust linear correlation with the inverse of wave age, spanning from developing to old seas. All scaled plume depths considered here are decreasing functions of wave age in developing seas.

Moreover, our study offers multiple parameterizations that effectively predict the observed variability in the penetration depth and surface area of bubble plumes. These parameterizations are based on readily available wind and wave statistics, making them valuable for applications in existing forecast models.

This study is the first to establish a direct relation between bubble plume penetration depth and whitecap coverage, revealing that the depth of bubble plumes is linked to their visible surface area. This finding is significant as it advocates the possibility of estimating the volume of bubble plumes by remote sensing. Moreover, it significantly expands the applicability of the recent theoretical framework introduced by *Callaghan* [2018] on predicting total wave breaking dissipation as a function of bubble plume penetration depth and whitecap coverage. In a companion paper, we examine dynamic relationships between the bubble plume statistics presented here and total wave breaking dissipation using our synchronized observations of bubble plumes and dissipation rates.

Finally, the parameterizations of bubble plume penetration depth presented in this study hold the potential for estimating the effective vertical transport of various particles, with a rising velocity on the order of few cm s^{-1} or less, induced by breaking surface waves. It is possible that the drifting SWIFT buoys used in this study aggregate in convergence zones with enhanced downwelling velocities, such that there would be a sampling bias in the interpretation of vertical transport [*Zippel et al.*, 2020]. However, no obvious convergence zones, windrows, or other organized surface fronts were observed during the PAPA data collection. Furthermore, the wind slip (1% of wind speed) of the buoys tends to cause a quasi-uniform sampling along a drift track even in the presence of surface features.

Data Availability Statement

The processed data presented in this study is available from the Dryad repository https://doi.org/10.5061/dryad.d7wm37q6z [*Derakhti*, Forthcoming 2023].

A: Echosounder calibration

The echosounder was calibrated using standard sphere calibration techniques *Demer et al.* [2015]. In this approach, a sphere of a known material is suspended below the beam of an echosounder. Since the sphere's properties are known, an analytical solution for the acoustic target strength can be calculated. The difference between the measured intensity of the scattering and the known scattering from the sphere at the transmit frequency is the total gain for the system. In post-cruise testing, a 38.1 mm diameter tungsten-carbide sphere with 6% cobalt binder was suspended 8 m below the transducers by a bridle connected to the hull

of the SWIFTs. The units were then deployed for 30-60 minutes on Lake Washington (Washington, USA), during which the attitude of the SWIFTS caused the suspended sphere to pass through the beam of the echosounder. The top 1% of targets at the sphere range, which are assumed to be those associated with the sphere being on-axis within the beam where the combined transmit-receive beampattern is highest, were then selected. The gain is then determined by solving for G_{cal} in the target strength equation using the known analytical solution for the target strength of the sphere.

In practice, a sphere is sized such that its scattering response contains no significant nulls within the bandwidth [*Demer et al.*, 2015; *Stanton and Chu*, 2008; *Lavery et al.*, 2017]. However, this is not feasible at 1 MHz since a small (< 1 cm) sphere would be required. Furthermore, for such a small sphere, the monofilament securing the sphere would contribute significantly to scattering, biasing the results [*Renfree et al.*, 2020]. Thus, we chose to use a larger sphere whose response is quite complex over the relevant frequency range. The pulse-compressed signal has sufficient bandwidth to clearly resolve the echo from the front interface and subsequent contributions from circumference waves. We, therefore, assumed that the peak of the pulse compressed signal represents the partial wave scattering cross-section of the sphere [*Stanton and Chu*, 2008]. This assumption is necessary given that a frequency-dependent calibration cannot be performed given the only output data product is a scattering intensity measurement representing the average within the range bin output by the ADCP.

At the time of this experiment, the firmware resulted in scattering that saturated the receiver in the high gain setting and saturated the receiver when using the calibration sphere at a range of ~8 m. There is, therefore, some uncertainty in the calibration gains and the field observations. We cannot conclusively state the magnitude of this uncertainty, but it is believed to be on the order of a few dB or less from the calibration gain. The justification for this statement is that the elastic response of the sphere is well resolved with the intensity (impulse response squared) of the signal from the first Rayleigh wave, approximately 9 dB smaller than the echo from the front interface of the sphere when the calibrations were performed at the lower gain setting. This is consistent with expectations based on the impulse response of a 38.1 mm tungsten carbine sphere [*Demer et al.*, 2015] and the arrival of the signal associated with the first Rayleigh wave. In the saturated data, the difference in intensity between the first Rayleigh wave and the saturated echo from the front interface was approximately 3 dB. Given the impulse response of the 38.1 mm sphere, this suggests that about 6 dB of scattering from the sphere had been clipped. When used in the high power setting, gains were applied assuming the clipped value was 6 dB. The practical effect of this uncertainty is to put consistent error bars on the volume scattering coefficients measured in the data. That is, all data are shifted similarly, making the absolute intensity of the backscattering more uncertain without impacting the relevant ranges between the thresholds.

The fact that scattering from the tungsten carbide sphere saturated at 8 m indicates the high gain setting almost certainly caused widespread saturation of signals in the upper portion ($\sim$ 10 m) of the water column when high densities of bubbles were present. A consequence of this is that the full dynamic range of volume backscattering is not resolved. Despite these challenges and uncertainties, we consider it preferable to present backscattering intensities in this approach to backscattering intensities expressed in decibels with reference value ground in physical measurements.

References

Al-Lashi, R. S., S. R. Gunn, and H. Czerski (2016), Automated processing of oceanic bubble images for measuring bubble size distributions underneath breaking waves, *J. Atmos. Oceanic Tech.*, *33*, doi:10.1175/JTECH-D-15-0222.1.

Anguelova, M. D., and P. Huq (2012), Characteristics of bubble clouds at various wind speeds, *J. Geophys. Res.: Oceans*, *117*, doi:10.1029/2011JC007442.

Banner, M., J. Gemmrich, and D. Farmer (2002), Multiscale measurements of ocean wave breaking probability, *J. Phys. Oceanogr.*, *32*, 3364–3375, doi:10.1175/1520-0485(2002) 032<3364:MMOOWB>2.0.CO;2.

Banner, M. L., A. V. Babanin, and I. Young (2000), Breaking probability for dominant waves on the sea surface, *J. Phys. Oceanogr.*, *30*, 3145–3160, doi:10.1175/1520-0485(2000) 030<3145:BPFDWO>2.0.CO;2.

Bassett, C., and A. Lavery (2021), Observations of high-frequency acoustic attenuation due to bubble entrainment at estuarine fronts, *Proceedings of Meetings on Acoustics*, *45*(1), 005,001, doi:10.1121/2.0001539.

Blenkinsopp, C. E., and J. R. Chaplin (2007), Void fraction measurements in breaking waves, *Proc. Royal Soc. A: Math, Phys. Eng. Sci.*, *463*, 3151–3170, doi:10.1098/rspa.2007.1901.

Brumer, S. E., C. J. Zappa, I. M. Brooks, H. Tamura, S. M. Brown, B. W. Blomquist, C. W. Fairall, and A. Cifuentes-Lorenzen (2017), Whitecap coverage dependence on wind and wave statistics as observed during so gasex and hiwings, *J Phys. Oceanogr.*, *47*, 2211–2235, doi:10.1175/JPO-D-17-0005.1.

Callaghan, A., G. de Leeuw, L. Cohen, and C. D. O'Dowd (2008), Relationship of oceanic whitecap coverage to wind speed and wind history, *Geophys. Res. Lett.*, *35*(23), doi:10. 1029/2008GL036165.

Callaghan, A. H. (2018), On the relationship between the energy dissipation rate of surface-breaking waves and oceanic whitecap coverage, *J. Phys. Oceanogr.*, *48*, 2609–2626, doi: 10.1175/JPO-D-17-0124.1.

Callaghan, A. H., G. B. Deane, and M. D. Stokes (2016), Laboratory air-entraining breaking waves: Imaging visible foam signatures to estimate energy dissipation, *Geophys. Res. Let.*, *43*, 11–320, doi:10.1002/2016GL071226.

Carter, D. (1982), Prediction of wave height and period for a constant wind velocity using the jonswap results, *Ocean Eng.*, *9*, 17–33, doi:10.1016/0029-8018(82)90042-7.

Chen, G., B. Chapron, R. Ezraty, and D. Vandemark (2002), A global view of swell and wind sea climate in the ocean by satellite altimeter and scatterometer, *J. Atm. and Oceanic Tech.*, *19*, 1849–1859, doi:10.1175/1520-0426(2002)019<1849:AGVOSA>2.0.CO;2.

Czerski, H., I. M. Brooks, S. Gunn, R. Pascal, A. Matei, and B. Blomquist (2022a), Ocean bubbles under high wind conditions–part 1: Bubble distribution and development, *Ocean Science*, *18*, 565–586, doi:10.5194/os-18-565-2022.

Czerski, H., I. M. Brooks, S. Gunn, R. Pascal, A. Matei, and B. Blomquist (2022b), Ocean bubbles under high wind conditions–part 2: Bubble size distributions and implications for models of bubble dynamics, *Ocean Science*, *18*, 587–608, doi:10.5194/os-18-587-2022.

Dahl, P. H., and A. T. Jessup (1995), On bubble clouds produced by breaking waves: An event analysis of ocean acoustic measurements, *J. Geophys. Res.: Oceans*, *100*, 5007–5020, doi:10.1029/94JC03019.

De Robertis, A., and I. Higginbottom (2007), A post-processing technique to estimate the signal-to-noise ratio and remove echosounder background noise, *ICES J. Mar. Sci.*, *64*(6), 1282–1291, doi:10.1093/icesjms/fsm112.

Deane, G. B., M. D. Stokes, and A. H. Callaghan (2016), The saturation of fluid turbulence in breaking laboratory waves and implications for whitecaps, *J. Phys. Oceanogr.*, *46*, 975–992, doi:10.1175/JPO-D-14-0187.1.

Deike, L. (2022), Mass transfer at the ocean–atmosphere interface: The role of wave breaking, droplets, and bubbles, *Ann. Rev. Fluid Mech.*, *54*, 191–224, doi:10.1146/ annurev-fluid-030121-014132.

Demer, D., L. Berger, M. Bernasconi, E. Bethke, K. Boswell, D. Chu, and Domokos, R. et al. (2015), Calibration of acoustic instruments, *ICES CRR No. 326*, doi:10.25607/OBP-185.

Derakhti, M. (Forthcoming 2023), Statistics of bubble plumes generated bybreaking surface waves [dataset], *Dryad*, doi:10.5061/dryad.d7wm37q6z.

Derakhti, M., and J. T. Kirby (2014), Bubble entrainment and liquid bubble interaction under unsteady breaking waves, *J. Fluid Mech.*, *761*, 464–506, doi:10.1017/jfm.2014.637.

Derakhti, M., and J. T. Kirby (2016), Breaking-onset, energy and momentum flux in unsteady focused wave packets, *J. Fluid Mech.*, *790*, 553–581, doi:10.1017/jfm.2016.17.

Derakhti, M., J. T. Kirby, F. Shi, and G. Ma (2016), Wave breaking in the surf zone and deep-water in a non-hydrostatic rans model. part 2: Turbulence and mean circulation, *Ocean Modelling*, *107*, 139–150, doi:10.1016/j.ocemod.2016.09.011.

Derakhti, M., M. L. Banner, and J. T. Kirby (2018), Predicting the breaking strength of gravity water waves in deep and intermediate depth, *J. Fluid Mech.*, *848*, doi:10.1017/jfm. 2018.352.

Derakhti, M., J. Thomson, and J. T. Kirby (2020a), Sparse sampling of intermittent turbulence generated by breaking surface waves, *J Phys. Oceanogr.*, *50*(4), 867–885, doi: 10.1175/JPO-D-19-0138.1.

Derakhti, M., J. T. Kirby, M. L. Banner, S. T. Grilli, and J. Thomson (2020b), A unified breaking-onset criterion for surface gravity water waves in arbitrary depth, *J. Geophys. Res.:Ocean*, *125*, doi:10.1029/2019JC015886.

Donelan, M., A. Babanin, E. Sanina, and D. Chalikov (2015), A comparison of methods for estimating directional spectra of surface waves, *Journal of Geophysical Research: Oceans*, pp. n/a–n/a, doi:10.1002/2015JC010808.

Felizardo, F., and W. Melville (1995), Correlation between ambient noise and the ocean surface wave field, *J. Phys. Oceanogr.*, *25*, 513–532.

Gemmrich, J. R., M. L. Banner, and C. Garrett (2008), Spectrally resolved energy dissipation rate and momentum flux of breaking waves, *J. Phys. Oceanogr.*, *38*, 1296–1312, doi:10. 1175/2007JPO3762.1.

Hsu, S. (2003), Estimating overwater friction velocity and exponent of power-law wind profile from gust factor during storms, *J. Waterway, Port, Coastal, Ocean Eng.*, *129*, 174–177, doi:10.1061/(ASCE)0733-950X(2003)129:4(174).

Iyer, S., K. Drushka, E. J. Thompson, and J. Thomson (2022), Small-scale spatial variations of air-sea heat, moisture, and buoyancy fluxes in the tropical trade winds, *Journal of Geophysical Research: Oceans*, *127*(10), e2022JC018,972, doi:https://doi.org/10.1029/ 2022JC018972, e2022JC018972 2022JC018972.

Kleiss, J. M., and W. K. Melville (2010), Observations of wave breaking kinematics in fetch-limited seas, *J. Phys. Oceanogr.*, *40*, 2575–2604, doi:10.1175/2010JPO4383.1.

Kleiss, J. M., and W. K. Melville (2011), The analysis of sea surface imagery for whitecap kinematics, *Journal of Atmospheric and Oceanic Technology*, *28*(2), 219–243.

Lamarre, E., and W. Melville (1991), Air entrainment and dissipation in breaking waves, *Nature*, *351*, 469–472.

Lavery, A., C. Bassett, G. Lawson, and J. Jech (2017), Exploiting signal processing approaches from broadband echosounder, *ICES J. Mar. Sci.*, *75*(8), 2262–2275, doi: 10.1093/icesjms/fsx155.

Liang, J., S. R. Emerson, E. A. D'Asaro, C. L. McNeil, R. R. Harcourt, P. P. Sullivan, B. Yang, and M. F. Cronin (2017), On the role of sea-state in bubble-mediated air-sea gas flux during a winter storm, *J. Geophys. Res.: Oceans*, *122*, 2671–2685, doi: 10.1002/2016JC012408.

Malila, M. P., J. Thomson, Breivik, A. Benetazzo, B. Scanlon, and B. Ward (2022), On the Groupiness and Intermittency of Oceanic Whitecaps, *Journal of Geophysical Research: Oceans*, *127*(1), e2021JC017,938, doi:https://doi.org/10.1029/2021JC017938.

Manasseh, R., A. V. Babanin, C. Forbes, K. Rickards, I. Bobevski, and A. Ooi (2006), Passive Acoustic Determination of Wave-Breaking Events and Their Severity across the Spectrum, *J. Atmos. and Oceanic Tech.*, *23*, 599–618, doi:10.1175/JTECH1853.1.

Medwin, H. (1977a), Counting bubbles acoustically: a review, *Ultrasonics*, *15*(1), 7–13, doi: https://doi.org/10.1016/0041-624X(77)90005-1.

Medwin, H. (1977b), In situ acoustic measurements of microbubbles at sea, *J. Geophys. Res.*, *82*(6), 971–976, doi:10.1029/JC082i006p00971.

Medwin, H., and C. Clay (1998), *Fundamentals of Acoustics Oceanography*, 138-141 pp., Academic Press, Boston, MA.

Melville, W. K. (1996), The role of surface-wave breaking in air-sea interaction, *Ann. Rev. Fluid Mech.*, *28*, 279–321.

Melville, W. K., and P. Matusov (2002), Distribution of breaking waves at the ocean surface, *Nature*, *417*, 58–63.

Melville, W. K., F. Veron, and C. J. White (2002), The velocity field under breaking waves: coherent structures and turbulence, *J. Fluid Mech.*, *454*, 203–233, doi:10.1017/S0022112001007078.

Monahan, E. C. (1969), Fresh water whitecaps, *J. Atmos. Sci.*, *26*, 1026–1029, doi:10.1175/1520-0469(1969)026<1026:FWW>2.0.CO;2.

Monahan, E. C., and I. Muircheartaigh (1980), Optimal power-law description of oceanic whitecap coverage dependence on wind speed, *Journal of Physical Oceanography*, *10*, 2094–2099, doi:10.1175/1520-0485(1980)010<2094:OPLDOO>2.0.CO;2.

Perlin, M., W. Choi, and Z. Tian (2013), Breaking waves in deep and intermediate waters, *Annual Review of Fluid Mechanics*, *45*(1), 115–145, doi:10.1146/annurev-fluid-011212-140721.

Phillips, O., F. Posner, and J. Hansen (2001), High range resolution radar measurements of the speed distribution of breaking events in wind-generated ocean waves: Surface impulse and wave energy dissipation rates, *J Phys. Oceanogr.*, *31*, 450–460, doi:10.1175/1520-0485(2001)031<0450:HRRRMO>2.0.CO;2.

Portilla, J., F. J. Ocampo-Torres, and J. Monbaliu (2009), Spectral partitioning and identification of wind sea and swell, *J. Atmosph. Oceanic Tech.*, *26*, 107–122, doi:10.1175/2008JTECHO609.1.

Rapp, R. J., and W. K. Melville (1990), Laboratory measurements of deep-water breaking waves, *Phil. Trans R. Soc. Lond. A*, *331*, 735–800, doi:10.1098/rsta.1990.0098.

Renfree, J. S., L. N. Andersen, G. Macaulay, T. S. Sessions, and D. A. Demer (2020), Effects of sphere suspension on echosounder calibrations, *ICES Journal of Marine Science*, *77*(7-8), 2945–2953, doi:10.1093/icesjms/fsaa171.

Scanlon, B., and B. Ward (2016), The influence of environmental parameters on active and maturing oceanic whitecaps, *J. Geophys. Res.*, *121*, 3325–3336, doi:10.1002/2015JC011230.

Schwendeman, M., and J. Thomson (2015a), Observations of whitecap coverage and the relation to wind stress, wave slope, and turbulent dissipation, *J. Geophys. Res.: Oceans*, *120*, 8346–8363, doi:10.1002/2015JC011196.

Schwendeman, M., and J. Thomson (2015b), A horizon-tracking method for shipboard video stabilization and rectification, *Journal of Atmospheric and Oceanic Technology*, *32*(1), 164–176.

Schwendeman, M., J. Thomson, and J. Gemmrich (2014), Wave breaking dissipation in a young wind sea, *J. Phys. Oceanogr.*, *44*, 104–127, doi:10.1175/JPO-D-12-0237.1.

Stanton, T. K., and D. Chu (2008), Calibration of broadband active acoustic systems using a single standard spherical target, *The Journal of the Acoustical Society of America*, *124*(1), 128–136, doi:10.1121/1.2917387.

Strand, K. O., Ø. Breivik, G. Pedersen, F. B. Vikebø, S. Sundby, and K. H. Christensen (2020), Long-term statistics of observed bubble depth versus modeled wave dissipation, *J. Geophys. Res.: Oceans*, *125*, e2019JC015,906, doi:10.1029/2019JC015906.

Sugihara, Y., H. Tsumori, T. Ohga, H. Yoshioka, and S. Serizawa (2007), Variation of whitecap coverage with wave-field conditions, *J Marine Sys.*, *66*, 47–60, doi:10.1016/j.jmarsys.2006.01.014.

Sullivan, P. P., and J. C. McWilliams (2010), Dynamics of winds and currents coupled to surface waves, *Ann. Rev. Fluid Mech.*, *42*, 19–42, doi:10.1146/annurev-fluid-121108-145541.

Sutherland, P., and W. K. Melville (2013), Field measurements and scaling of ocean surface wave-breaking statistics, *Geophys. Res. Let.*, pp. 3074–3079, doi:10.1002/grl.50584.

Terrill, E. J., W. K. Melville, and D. Stramski (2001), Bubble entrainment by breaking waves and their influence on optical scattering in the upper ocean, *J. Geophys. Res.: Oceans*, *106*, 16,815–16,823, doi:10.1029/2000JC000496.

Thomson, J. (2012), Wave breaking dissipation observed with SWIFT drifters, *J. Atmos. Oceanic Technol.*, *29*, 1866–1882, doi:10.1175/JTECH-D-12-00018.1.

Thomson, J., and A. Jessup (2009), A fourier-based method for the distribution of breaking crests from video observations, *J. Atmos. Ocean. Tech.*, *26*, 1663–1671, doi:10.1175/2009JTECHO622.1.

Thomson, J., M. S. Schwendeman, S. F. Zippel, S. Moghimi, J. Gemmrich, and W. E. Rogers (2016), Wave-breaking turbulence in the ocean surface layer, *J. Phys. Oceanogr.*, *46*, 1857–1870, doi:10.1175/JPO-D-15-0130.1.

Thomson, J., J. B. Girton, R. Jha, and A. Trapani (2018), Measurements of directional wave spectra and wind stress from a wave glider autonomous surface vehicle, *J. Atm. Oceanic Tech.*, *35*(2), 347–363, doi:10.1175/JTECH-D-17-0091.1.

Thomson, J., M. Moulton, A. de Klerk, J. Talbert, M. Guerra, S. Kastner, M. Smith, M. Schwendeman, S. Zippel, and S. Nylund (2019), A new version of the swift platform for waves, currents, and turbulence in the ocean surface layer, in *IEEE/OES Workshop on Currents, Waves, and Turbulence Measurements*.

Thorpe, S. (1982), On the clouds of bubbles formed by breaking wind-waves in deep water, and their role in air-sea gas transfer, *Phil. Tran. R. Soc. Lond. A*, *304*, 155–210, doi:10.1098/rsta.1982.0011.

Thorpe, S. (1986), Measurements with an automatically recording inverted echo sounder; aries and the bubble clouds, *J. Phys. Oceanogr.*, *16*, 1462–1478, doi:10.1175/1520-0485(1986)016<1462:MWAARI>2.0.CO;2.

Thorpe, S. (1992), Bubble clouds and the dynamics of the upper ocean, *Quart. J. Roy. Meteor. Soc.*, *118*, 1–22, doi:10.1002/qj.49711850302.

Trevorrow, M. (2003), Measurements of near-surface bubble plumes in the open ocean with implications for high-frequency sonar performance, *J. Acous. Soc. Am.*, *114*(5), 2672–2684, doi:10.1121/1.1621008.

Vagle, S., and D. Farmer (1992), Measurements of bubble-size distributions by acoustical backscatter, *J. Ocean. Atmos. Tech.*, *9*(5), 630–644, doi:10.1175/1520-0426(1992)009<0630:TMOBSD>2.0.CO;2.

Vagle, S., and D. Farmer (1998), A comparison of four methods for bubble size and void fraction measurements, *IEEE Journal of Oceanic Engineering*, *23*(3), 211–222, doi:10.1109/48.701193.

Vagle, S., C. McNeil, and N. Steiner (2010), Upper ocean bubble measurements from the ne pacific and estimates of their role in air-sea gas transfer of the weakly soluble gases nitrogen and oxygen, *J. Geophys. Res.: oceans*, *115*, doi:10.1029/2009JC005990.

Wang, D. W., H. W. Wijesekera, E. Jarosz, W. J. Teague, and W. S. Pegau (2016), Turbulent diffusivity under high winds from acoustic measurements of bubbles, *J. Phys. Oceanogr.*, *46*, 1593–1613, doi:10.1175/JPO-D-15-0164.1.

Yelland, M., P. Taylor, I. Consterdine, and M. Smith (1994), The use of the inertial dissipation technique for shipboard wind stress determination, *J. Atmos. Ocean. Tech.*, *11*, 1093–1108.

Zhao, D., and Y. Toba (2001), Dependence of whitecap coverage on wind and wind-wave properties, *J. Oceanogr.*, *57*, 603–616, doi:10.1023/A:1021215904955.

Zippel, S. F., T. Maksym, M. Scully, P. Sutherland, and D. Dumont (2020), Measurements of enhanced near-surface turbulence under windrows, *Journal of Physical Oceanography*, *50*(1), 197–215, doi:10.1175/JPO-D-18-0265.1.